CRYSTALLIZATION CHARACTERISTICS IN CO-BASED MAGNETIC AMORPHOUS NANOCOMPOSITE ALLOYS

by

ALICIA G. KOENIG

GREGORY THOMPSON, COMMITTEE CHAIR
TIM MEWES
LIN LI
MARK WEAVER
YU LEI

A DISSERTATION

Submitted in partial fulfillment of the requirements
for the degree of Doctor of Philosophy
in the Department of Metallurgical
and Materials Engineering
in the Graduate School of
The University of Alabama

TUSCALOOSA, ALABAMA

2022

ABSTRACT

This document will describe analytical procedures for the microstructural characterization of Co-based soft magnetic amorphous nanocomposite materials and the evolution of that microstructure after heat treatment. Atom probe tomography analysis of these alloys reveals increased chemical diffusion with additional solute content, as well as a reduction in defects in the crystalline phase. It was confirmed that Co and Fe partition preferentially to the crystalline phase, and that other elements (B, Si, Nb, Mn) segregate to the amorphous matrix. It was found that a combination of FCC/HCP structures were the basis for the crystalline phase.

Differential scanning calorimetry was used to evaluate the characteristics of phase transition as a function of solute content, revealing an increase in the necessary energy for the formation of the primary crystallization phase with higher solute concentrations. From this data, the primary crystallization temperature was estimated and anneals were performed at a temperature just below that to slow the kinetics of crystallite nucleation and growth. Postmortem atom probe tomography and transmission electron microscopy data revealed that the alloy undergoes a constant nucleation condition, and that the added solute content suppresses the nucleation and growth behavior of both the primary and secondary crystalline phases.

Finally, as strain annealing has been shown to improve the desired magnetic properties in these alloys, but the mechanisms are not yet understood, a method for applying digital image correlation techniques to tensile testing in an *in situ* tensile testing environment is described. This will establish precedent for applying these analyses to *in situ* tensile testing of sputter-deposited magnetic alloys, and eventually to *in situ* thermomechanical testing.

DEDICATION

This work is gratefully dedicated to my husband, Thomas, whose patience, insight, and love have made my graduate studies possible. I will be proud to share the title of ‘Dr. Koenig’ with him as he defends his own graduate work.

LIST OF SYMBOLS

$\boldsymbol{B}$	magnetic field density
β	heating rate
E_{loss}	energy loss (due to magnetic switching)
$\boldsymbol{H}$	magnetic field strength
H_C	magnetic coercivity
N	number of inductor loops
Δt	change in time
$\boldsymbol{V}$	volume
ε	electromagnetic force
ϕ	magnetic flux
$\Delta\phi$	change in magnetic flux
μ	magnetic permeability
ρ	density (atoms/nm^3)
ρ_{number}	number density (crystallites/m^3)

LIST OF ABBREVIATIONS

APT	atom probe tomography
DIC	digital image correlation
DSC	differential scanning calorimetry
ePDF	electron pair distribution function
FCC	face centered cubic
FFT	fast Fourier transform
FIB	focused ion beam
HCP	hexagonal close packed
MANC	magnetic amorphous nanocomposite
PDF	pair distribution function
PT	particle tracking
ROI	region of interest
SAD/SAED	selected area electron diffraction
SEM	scanning electron microscopy
STEM	scanning transmission electron microscopy
SRO	short range order
TEM	transmission electron microscopy
XRD	x-ray diffraction

ACKNOWLEDGEMENTS

A PhD dissertation is a culmination of so much work and cannot be brought to fruition alone. There are many people who supported me in pursuit of my goals. First and foremost to be thanked is my advisor, Dr. Greg Thompson, for both his dedication to his students and for challenging me to grow as a scientist, writer, and speaker. Further, the contributions of Dr. Ron Noebe and Dr. Alex Leary have driven me to improve in my writing and presentation skills, and I am incredibly grateful. I would also like to thank the members of my committee for their time, support, and flexibility as I work towards the completion of my studies. Finally, I would like to acknowledge the AARC staff for their assistance and tireless efforts towards supporting student researchers, at all hours of the day and night.

In addition to the group of scientists who have helped shape the path of my research, I would also like to thank my "Inner Circle" of friends for their emotional support, friendship, and love. Thank you to Tara Heiser, Emily Harvey, and Elizabeth Moon.

Finally, this work was supported by NASA CAN 80NSSC18M0023. Additional support for this work came from the NASA Advanced Air Transport Technology Project, Electrified Aircraft Powertrain Technologies Subproject, and Army Research Office grant W911NF-17-1-0528.

CONTENTS

LIST OF TABLES

LIST OF FIGURES

CHAPTER 1: INTRODUCTION

1.1 Magnetic Materials in Modern High-Frequency AC Applications

The generation, transformation, and storage of energy is a major source of pollution, largely due to energy losses in components. In particular, the improvement of electric propulsion capabilities is of high priority in efforts to reduce air pollution generated by the combustion of fossil fuels [1]. However, this technology is currently limited by the weight of the required components [2]. Consequently, components of electronic motors must be improved in size, weight, and power density while remaining stable at high operating temperatures.

The optimization of magnetic core alloys offers two avenues for the reduction of weight in electric motors. First, the reduction of power losses which occur during the switching of magnetic field orientations would result in a higher power density per unit mass [3]. Second, an increase in acceptable operating temperatures without core degradation would reduce the need for heavy cooling systems [4].

The operating principle for the generation and transformation of power via magnetic interactions can be summarized via Faraday's law of inductance: a changing magnetic flux $\Delta\phi$ in a system induces an opposing electromotive force (EMF, ε) in the system circuitry,

$$\varepsilon = -N\frac{\Delta\phi}{\Delta t} \tag{1.1}$$

where N is the number of inductor loops and Δt is the change in time.

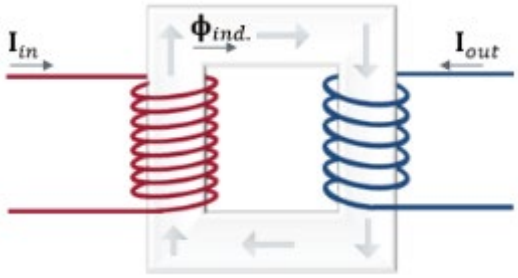

Figure 1.1 Simplified diagram of an AC power transformer, adapted from [5].

Faraday's law is the driving principle for alternating current (AC) electric motors, generators, and transformers to function. In motor applications, electrical power is converted to mechanical power through the rotation of a coil with respect to a magnetic field, with the resultant EMF generating a torque. In contrast, transformers facilitate the conversion of electric power between isolated circuits, generating both a current and voltage in secondary windings coupled by an inductor core (see: **Figure 1.1**) [5], [6].

These processes for the generation and conversion of energy are dependent on the changing of the magnetic flux, $\phi = \vec{B} \cdot \vec{A}$ (the magnetic field $\vec{B}$ through the area $\vec{A}$) in the magnetic core over time. The magnetic field $\vec{B}$ is a function of the applied field strength $\vec{H}$ and the magnetization of the material $\vec{M}$, i.e. $\vec{B} = \mu_0(\vec{H} + \vec{M})$, where μ_0 is the permeability of free space. It is this interaction which drives overall losses as the losses in the magnetic material occur in magnetization $\vec{M}$. For transformers, the direction of the magnetic flux in the inductor core is reversed with each switching cycle of the AC power supply. There is a consequential loss of energy for each cycle, as the energy lost during reversal of the magnetization is released into the system as heat.

The process of magnetic switching in a ferromagnetic material can be described by the magnetic hysteresis curve, where the magnetic flux density $\boldsymbol{B}$ is plotted as a function of the

applied magnetic field strength $\boldsymbol{H}$ within the material in electric motors, generators, etc. $\boldsymbol{H}$ is generated by moving charges i.e. current; thus, when the current direction switches, so do $\boldsymbol{H}$ and $\boldsymbol{B}$. A significant portion of energy losses are directly related to this switching behavior. This energy loss can then be described as follows:

$$E_{loss} = \int_V \left[\oint (\boldsymbol{H}\ d\boldsymbol{B}) \right] d\boldsymbol{V} \qquad 1.2$$

where energy loss due to magnetic hysteresis is proportional to the area inside the hysteresis loop.

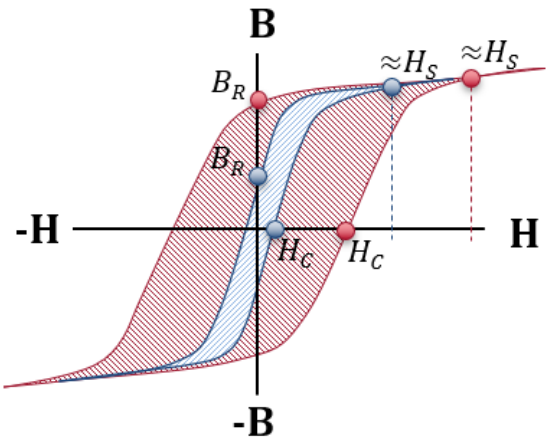

Figure 1.2 Example hysteresis loops for a hard (red) and soft (blue) magnetic material.

The magnetic properties of a material describe the ease of reversal of the magnetic field direction. Examination of the anatomy of the B-H plot displayed in **Figure 1.2** shows the influence of some key magnetic properties. Key in the reduction of the loop size and thus in energy loss is the magnetic coercivity, H_C, or the magnitude of the field strength $\boldsymbol{H}$ required to demagnetize a magnetically saturated ferromagnetic material. Materials with a low coercivity are classified as having "soft" magnetic properties; likewise, materials with a high coercivity are considered to be "hard" magnets. For the purpose of reducing energy losses in transformer cores during high frequency AC switching, soft magnetic materials are superior.

1.2 The History of Soft Magnetic Materials

Typically, soft magnetic alloys are used because of their notably low magnetic coercivity, which better facilitates the ease of magnetic switching when compared to permanent magnets. The industry standard soft magnetic alloys for transformer cores are typically soft ferrites and Si steels [4]. These are readily manufactured via currently established infrastructure. However, these alloys suffer high losses when operating at high frequencies [7], often due to the subjection of these components to non-sinusoidal excitations in these operating conditions. Generally, modern power electronics operate at high frequencies, allowing a faster dynamic response to changes in current and generally permit smaller and lighter magnetic components [8]. Nanocrystalline and amorphous alloys have been shown to have lower losses when operating at higher frequencies [7], making them ideal candidates to replace traditional soft magnetic alloys.

For this reason, several classes of nanocrystalline/amorphous alloys are currently being investigated for high frequency applications [9]–[13]. An ideal alloy would maintain a high magnetic saturation value while also being able to switch magnetization direction with ease. There are many classes of nanocrystalline/amorphous alloys, which have been in commercial development since Yoshizawa et. al. [14] introduced a modification of a common Fe-Si-B amorphous alloy via the addition of Nb and Cu dopants, improving the microstructural stability up to 120°C. This led to the development of a wide variety of similarly designed alloys including FINEMET, VITROPERM, NANOPERM, and HITPERM [15]–[20]. The last several decades of research combined have resulted in a collective compendium of solvent/solute selections and their relationships with microstructural and magnetic properties. The most general of these relationships in these magnetic amorphous nanocomposites (MANCs) are summarized briefly below.

The fundamental microstructural principle in minimizing coercivity is the average grain size. Coercivity increases with increasing anisotropy energies, and decreases with increasing permeability, as discussed in [21]. These properties are in turn heavily influenced by exchange coupling behavior between magnetic domains and magnetic anisotropy energies [21], [22]. On a macroscopic scale, magnetic exchange coupling behavior is strongly influenced by the composition and morphology of phases present in an alloy [23]. **Figure 1.3** shows the influence of grain size on coercivity in a number of alloy systems. The smaller grain size regime is dominated by this magnetic exchange coupling length mechanism, which at this point becomes larger than the average grain size, increasing the ease of switching. Similarly, macroscopic anisotropies are dependent on orientations and structures of crystallites. It has been shown that orientations and textures of polycrystalline soft magnets can directly influence hysteresis-related power loss as the global averaging of local anisotropies reduces the global magnetocrystalline anisotropy in the core [24]. The combination of these mechanisms promotes an ease of switching both of individual magnetic domains and of the global magnetic orientation.

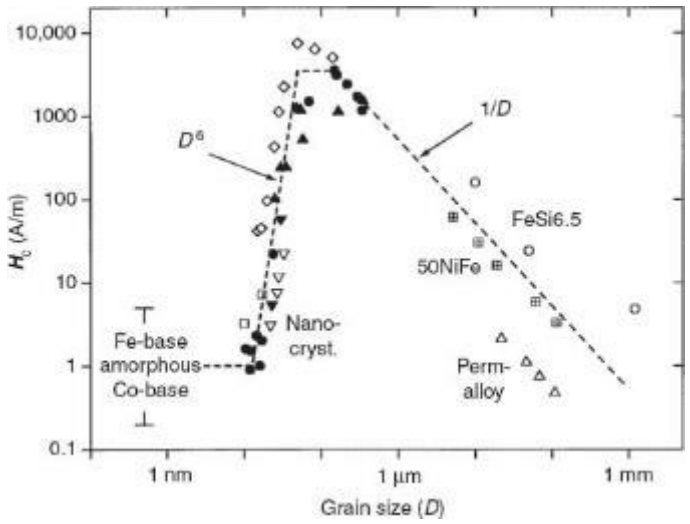

Figure 1.3 Coercivity vs grain size. From [23].

To promote these stable nanocrystalline microstructures while preserving a high saturation magnetization, these alloys are necessarily precisely engineered multicomponent systems with many interwoven metallurgical mechanisms. MANCs are typically rich in strongly ferromagnetic species, i.e. Fe, Ni, and Co, while also containing a number of solute alloying species. Multiple solute components are introduced to provide a specific benefit to the alloy properties and stabilize the desired nanostructure. Glass formers, such as B, Si, are typically included to promote the amorphous phase and to stabilize the amorphous matrix after annealing. Growth impeders, typically early transition metals such as Zr, Hf, and Nb, serve to limit grain growth during anneal, stabilizing the nanocrystalline sized grains and maintaining high temperature stability (particularly important due to the operating conditions experienced by magnetic cores in AC motors).

MANCs are characterized by nanocrystallites, on the order of <50 nm, embedded within an amorphous matrix, allowing the material to benefit from the increased resistivity of the amorphous phase (which minimizes the generation of eddy currents leading to losses) while maintaining grain size well below the exchange length through intermediate temperatures [4]. Many of the early MANCs were Fe-rich. In order to facilitate the formation of such a fine microstructure, it has been speculated that nucleation of crystallites in Fe-based soft magnetic materials can be enhanced via the addition of Cu [21]. In the initial stages of annealing, Cu diffuses and precipitates out of solution to form a fine dispersion of Cu-rich clusters. Because Cu is substituted for Fe, the clustering of Cu creates a chemical landscape defined by fluctuations in Fe concentration. Consequently, between Cu-rich clusters exist Fe-rich regions which then serve as nucleation sites for BCC Fe-Si. This results in a fine dispersion of nucleation sites which are activated at a very high rate, and then proceed to grow at a diffusion-limited rate [25].

Traditionally, many magnetic amorphous nanocomposite alloys are fabricated via a process of spin melting. The individual elemental components are combined in a vat, melted, and mixed to form a solid solution. The mixture is then fed through a nozzle and rapidly quenched to lock in the glassy solid solution microstructure. In the case of the spin-melt process, this quenching is done via contact with a chilled, rapidly spinning drum pressed against the nozzle. The material is subsequently ejected from the drum in the form of a long, thin ribbon of amorphous material which can be shaped and heat-treated as necessary. The advantage of this manufacturing method is the rapid quenching of the alloy in a nearly homogeneous solid solution, usually resulting in a fine dispersion of nucleation sites which are necessary for the formation of the desired nanoscale crystallites.

Clearly there have been numerous studies on multiple alloy systems subjected to various processing methods. The majority focus on the influence of modifications to a specimen (alloying, solute introduction, annealing treatments, etc.) on the magnetic response of the specimen. However, in complex multicomponent alloy systems such as these it becomes problematic to pinpoint and define isolated relationships and interactions between chemistry, processing, and magnetic response. This makes it difficult to accurately predict the effect of any specific modification on magnetic properties, limiting further progress to chance rather than design by intent.

The approach described in this document will fully characterize the microstructural and chemical segregation behavior of a case-study alloy during heat treatment under various circumstances, thereby building a fundamental understanding of the influence of solute content and processing conditions on crystallization kinetics and resulting phase behavior. The author also hopes to establish a precedent for characterization of chemical partitioning, nucleation and

growth behavior, and tensile response in MANCs. With these interactions well-defined, designing further modifications can be made more intentional, thereby driving the rate of material optimization ever higher.

1.3 Materials Selection and Characterization Methodology

This document will describe the characterization methods used to determine the influence of solute content on atomic ordering, nucleation and growth, diffusion kinetics, and resultant microstructural features as pertaining to magnetic behavior. To fully examine these relationships, a combination of transmission electron microscopy (TEM) bright-field imaging and diffraction coupled with atom probe tomography (APT) will be employed to examine the chemical makeup and partitioning preferences of the various species within this alloy. Differential scanning calorimetry (DSC) will be used to give insights into the nucleation and growth behavior of the alloy. Using a combination approach of analytical techniques, detailed information on the quantity and structure of nucleation sites and the evolution of this structure during anneal will be determined.

1.3.1 Chemical and structural characterization

Atom probe tomography (APT) is a high-resolution, chemically sensitive 3D imaging technique for state-of-the-art materials characterization and analysis at the atomic scale. This technique has been used to characterize soft magnetic materials since very early in their history [26], [27]. Due to the high degree of chemical sensitivity, it is an ideal technique to apply to alloys with complex chemistries. APT has been applied to soft magnetic materials to describe chemical clustering [28], [29], phase separation [30]–[32], and even to examine nucleation and growth behavior [33]. Another factor is the scale of the region of interest (ROI) in an APT specimen. Typical specimen volumes are on the order of $>10^6$ nm^3. This is ideal for examining

the typical features in MANCs, where precipitates have a diameter of <50 nm; in any single specimen it is virtually guaranteed to find evidence of both phases, yet the resolution is still high enough to further capture much finer clustering behavior in the same study [34]. The APT work in this dissertation was used to describe not only the chemical composition of the constituent phases, but also used isodensity surface analyses to examine the degree of crystallinity and the presence of defects in the alloy as a function of solute content (see: Chapter 2).

The pair distribution function (PDF) is a graphical representation of the average probability of encountering an atom as a function of radial distance from some arbitrary reference atom. A measured PDF can therefore deliver information on first and second nearest neighbor distances and preferred atomic bonding angles in amorphous materials The arrangement of constituent atoms in an idealized, perfectly amorphous material would be that of perfect disorder. However, due to preferential behavior in atomic bond lengths and angles, there is always some degree of pattern repetition on a very small scale. This leads to a short-range ordering phenomenon in amorphous materials. The characteristic that differentiates amorphous materials from crystalline materials is not the presence of order, but the length scale over which ordering occurs. Crystalline materials are marked by the presence of long-range ordering, which can be entirely described by the translation and reflection of an atomic motif along some lattice framework. In contrast, order in amorphous materials is limited to discrete regions of <1-2nm in size, or the length scale encompassing the first several nearest neighbors.

Diffraction experiments have long been known to contain information from which the PDF can be extrapolated [35]–[37]. Several methods of extracting this information from electron diffraction patterns as generated by TEM are currently publicly available [38]–[40]. The ePDFSuite software package developed by NanoMEGAS [41] was selected for the purposes of

this study. By using calculations derived from the ePDFSuite, information about short-range ordering in the amorphous phases of the alloy series can be quantified.

To gather data with appropriate signal for electron PDF (ePDF) analysis, several factors must be considered. The ePDF is a function of diffracted intensity, which is itself a function of the scattering vector. To capture data with an appropriate signal to noise ratio, several methods may be used either separately or in combination. The data may be collected as a series of diffraction patterns which are then averaged together. Additionally, information from higher scatting vectors is typically sparser than that from low scattering vectors. To further strengthen the signal to noise ration (SNR), as well as to transform the data to a more appropriate form for ePDF calculations, the diffraction pattern data will then be subjected to a radial averaging procedure. This radially averaged intensity profile can then be used to calculate the atomic scattering factor, reduced interference function, reduced density function, and finally the ePDF. This ePDF provides insight into the distribution of atoms around an arbitrary central atom, and thus insight into potential ordering parameters of the amorphous phase. To read more about the experimental setup and parameters used for data collection in this study, the reader is referred to Appendix A.

1.3.2 *In situ* characterization

Differential scanning calorimetry (DSC) is an experimental method for characterizing changes in enthalpy as a function of temperature and time. The measured change in enthalpy can then be related to the physical and chemical changes that the specimen undergoes. This makes DSC an excellent method for studying phase transitions in materials. Of particular interest to this work is the ability to examine the temperature at which phase transitions occur as well as the activation energies required for those transitions. Using the Kissinger method [42], [43], the

activation energy for partial crystallization of an alloy can be calculated using equation 1.3 below

$$\ln\left(\frac{\beta}{T_p^2}\right) = \ln\left(\frac{AR}{Q}\right) - \left(\frac{1}{T_p}\right)\left(\frac{Q}{R}\right) \quad 1.3$$

where β is the linear heating rate, T_p is the temperature at the peak maximum in the DSC curve, where A, R, and Q are constants. Because we know the value of R, the ideal gas constant, and we can measure β and T_p (the heating rate and temperature of the peak location, respectively), this equation can be rearranged such that the activation energy Q is simply equal to the ideal gas constant multiplied by the slope of the line

$$\ln\left(\beta/T_p^2\right) = C - Q/RT_p \quad 1.4$$

for a series of experimentally measured (β, T_p) pairs (or $Q \cong m * R$) . Thus, by applying the linear regression of $\ln\left(\beta/T_p^2\right)$ vs. $1/T_p$ for several different heating rates, the activation energy can be calculated (to see an example of this plot, the reader is referred to Figure 3.1). This allows us to compare the crystallization behaviors, including ease of crystallization and crystallization temperature, as a function of alloy chemistry. This information can then be used to inform our anneal temperature and durations, as well as to contextualize structural and chemical characterization findings.

1.3.3 Digital image correlation

As will be discussed in the following section (1.3.4), the alloy series selected for this study has shown a relationship between magnetic properties and the application of a mechanical strain during the annealing treatment. For this reason, examination of the mechanical and microstructural responses during strain annealing would elucidate the underlying mechanisms of this magnetic response. A potential platform for such a study would be the development of

microelectromechanical system (MEMS) devices with the potential for inducing simultaneous thermal and mechanical loading within a TEM [44]. While the development of these devices and associated techniques are still in the early stages, they could in principle be applied to the characterization of MANCs with the purpose of elucidating nucleation and crystallization behavior during thermomechanical annealing of amorphous soft magnets.

Of course, data collection and analysis for such an experiment is a task unto itself. A video file for a single mechanical loading experiment could include hundreds or thousands of images, an impossible task for a single researcher to comb through with any efficiency. The use of automated data processing methods utilizing computer vision is a critical next step in the process.

Digital image correlation (DIC) is an analytical technique for mapping surface deformation [45]. This technique is applied to an image series of a specimen undergoing mechanical testing, allowing the user to map the displacement of discrete points within a specified region of interest (ROI). This data can then be used to generate maps of deformations, strains, velocities, etc. in that sample as a function of time. DIC was originally developed for the analysis of optical data; application of this technique becomes problematic when applied to electron microscopy, where imaging methods and signal processing become more complex due to the issues associated with diffraction contrast [46]. The optimization of this technique for the purpose of applying to *in situ* data of thermomechanical testing via MEMS in a TEM would be a great step towards understanding the role of strain annealing in MANCs.

1.3.4 Case study alloy

The alloy system selected for analysis is a series of Co-based nanocomposite alloys, which are of particular interest in high-temperature environments due to their increase in the

Curie temperature as compared to Fe-based alloys [19]. The nanocomposite alloy series $Co_{(80-x-y)}Fe_xMn_yB_{14}Si_2Nb_4$, has previously been shown by Leary *et. al.* [47] to exhibit remarkable changes in magnetic permeability as the ratios of Co-Fe-Mn are adjusted. This relationship has been postulated to be attributed to a number of different factors. Broadly speaking, the reduction of grain size in soft magnetic alloys has long been known to result in a lower coercivity and higher permeability, particularly below the threshold at which it becomes shorter than the magnetic exchange length [23]. Similarly, shorter inter-crystallite distances have also been shown to reduce coercivity in ferromagnetic nanocrystallites [48]. Furthermore, crystal structure has also been shown to have an effect on permeability, as the minimization of magneto-crystalline anisotropies increases permeability [21]. Finally, the composition of the alloy also influences its magnetic properties, largely via its influence on one or more of the above characteristics [29], [49], [50].

1.4 Dissertation Objectives

Considering the extent of contributing factors (chemistry, phase, microstructure), this work has been structured to examine the microstructural evolution under a variety of circumstances. Three objectives were set for evaluation:

1. Develop a precedent for identifying the microstructure and associated chemical partitioning in Co-Fe-Mn based alloys under standard annealing treatment conditions and identify the effect(s) that solute content has on these properties.
2. Develop a precedent for identifying the nucleation and growth mechanics that define the microstructural evolution of the alloy during annealing and evaluate whether Mn solute content has an effect on the behavior of these mechanisms

3. Develop capabilities for the *in-situ* thermomechanical response to strain annealing in the TEM environment.

1.5 Dissertation Structure

This document has been organized and formatted as an "article-style" dissertation. The following three chapters each contain an individual journal article that has been published or is currently being prepared for publication in peer reviewed journals. The final chapter will be a summary of results and a conclusion to the dissertation. Each chapter will include a unique bibliography.

1.5.1 Chapter 2 – Overview

This chapter characterizes the microstructure and phase formation of the alloys when heat treated in vacuum using the established standard conditions of 520°C for 20 minutes. APT analysis indicated that the degree of chemical partitioning was increased as a function of Mn content. Further analysis of APT data revealed that additional Mn also may have improved the degree of crystallinity in the Co-rich phase, with a higher density of atoms/unit volume indicating the presence of fewer vacancies and other defects.

1.5.2 Chapter 3 – Overview

This chapter describes the nucleation and growth process of the nanocrystallites to identify the influence of devitrification mechanisms on crystallite volume fraction and morphology. Samples were annealed at 400°C, just below the measured primary crystallization temperature, to slow kinetics for *ex situ* examination of the process of nucleation and growth.

The as-cast and annealed samples were examined via a combination approach using DSC, APT, and TEM. It was concluded that the addition of Mn slowed nucleation rates in this alloy system.

1.5.3 Chapter 4 – Overview

This chapter will describe efforts to establish DIC as a path forward in the examination of MANCs by evaluating the effects of strain annealing via the *in situ* mechanical deformation of amorphous thin films in a TEM environment. It was found that the application of a fine speckle pattern, created via the application of thermal shock, improved the ability of the analysis software to successfully map frames. This technique can be applied to MANC thin films in the future as techniques for sample preparation and MEMS operation are improved.

1.5.4 Chapter 5 – Overview

This chapter will conclude the dissertation with a brief summary of the results, discussion, and recommendations for future research.

References

[1] L. Gipson, "NASA Tests Machine to Power the Future of Aviation Propulsion," *NASA*, Aug. 09, 2021. http://www.nasa.gov/aeroresearch/nasa-tests-machine-to-power-the-future-of-aviation-propulsion (accessed Apr. 11, 2022).

[2] "Electrified Aircraft Propulsion (EAP)," *Glenn Research Center | NASA*. https://www1.grc.nasa.gov/aeronautics/eap/ (accessed Apr. 18, 2022).

[3] R. Jansen, C. Bowman, A. Jankovsky, R. Dyson, and J. Felder, "Overview of NASA Electrified Aircraft Propulsion (EAP) Research for Large Subsonic Transports," in *53rd AIAA/SAE/ASEE Joint Propulsion Conference*, American Institute of Aeronautics and Astronautics, 2017. doi: 10.2514/6.2017-4701.

[4] J. M. Silveyra, E. Ferrara, D. L. Huber, and T. C. Monson, "Soft magnetic materials for a sustainable and electrified world," *Science*, vol. 362, no. 6413, Oct. 2018, doi: 10.1126/science.aao0195.

[5] "Induction Motors." http://hyperphysics.phy-astr.gsu.edu/hbase/magnetic/indmot.html (accessed Jan. 06, 2020).

[6] O. Tola, O. James, J. Ambafi, A. Yahaya, Enesi, Shadrack, A. Adefemi., "The Application of Computer Programming in Transformer Design," *AU J. Technol.*, vol. 16, pp. 231–240, May 2013.

[7] A. Leary, P. R. Ohodnicki, and M. McHenry, "Soft Magnetic Materials in High-Frequency, High-Power Conversion Applications," *JOM J. Miner. …*, vol. 64, Jul. 2012, doi: 10.1007/s11837-012-0350-0.

[8] P. T. Krein, "1 - Introduction," in *Power Electronics Handbook (Fourth Edition)*, M. H. Rashid, Ed. Butterworth-Heinemann, 2018, pp. 1–12. doi: 10.1016/B978-0-12-811407-0.00001-5.

[9] A. Srivastava, K. Cole, A. Wadsworth, T. Burton, C. Mewes, T. Mewes, G. B. Thompson, R. Noebe, A. M. Leary., "Broadband characterization of stress induced anisotropy in nanocomposite Co74.6Fe2.7Mn2.7Nb4Si2B14," *J. Magn. Magn. Mater.*, vol. 500, p. 166307, Apr. 2020, doi: 10.1016/j.jmmm.2019.166307.

[10] Y. Krimer, N. Aronhime, P. Ohodnicki, and M. E. McHenry, "Prediction of good glass forming ability in amorphous soft magnetic alloys by thermocalc simulation with experimental validation," *J. Alloys Compd.*, vol. 814, p. 152294, Jan. 2020, doi: 10.1016/j.jallcom.2019.152294.

[11] A. Masood H. A. Baghbaderani, V. Ström, P. Stamenov, P. McCloskey, C. Ó. Mathúna, S. Kulkarni., "Fabrication and soft magnetic properties of rapidly quenched Co-Fe-B-Si-Nb ultra-thin amorphous ribbons," *J. Magn. Magn. Mater.*, vol. 483, pp. 54–58, Aug. 2019, doi: 10.1016/j.jmmm.2019.03.079.

[12] J. Hwang, H. Lee, and S. Yi, "Formation and Magnetic Properties of Nanocomposites in Rapidly Solidified Fe42Ni41.7C7Si4.5B3.9P0.9 (at%) Ribbons," *Met. Mater. Int.*, vol. 25, pp. 1–8, Jan. 2019, doi: 10.1007/s12540-018-0163-y.

[13] B. Zang R. Parsons, K. Onodera, H. Kishimoto, A. Kato, A. C. Y. Liu, K. Suzuki, "Effect of heating rate during primary crystallization on soft magnetic properties of melt-spun Fe-B alloys," *Scr. Mater.*, vol. 132, pp. 68–72, Apr. 2017, doi: 10.1016/j.scriptamat.2017.01.030.

[14] Y. Yoshizawa, K. Yamauchi, T. Yamane, and H. Sugihara, "Common mode choke cores using the new Fe-based alloys composed of ultrafine grain structure," *J. Appl. Phys.*, vol. 64, no. 10, pp. 6047–6049, Nov. 1988, doi: 10.1063/1.342150.

[15] K. Suzuki, M. Kikuchi, A. Makino, A. Inoue, and T. Masumoto, "Changes in Microstructure and Soft Magnetic Properties of an Fe86Zr7B6Cu1 Amorphous Alloy upon Crystallization," *Mater. Trans. JIM*, vol. 32, no. 10, pp. 961–968, 1991, doi: 10.2320/matertrans1989.32.961.

[16] M. A. Willard, J. C. Claassen, R. M. Stroud, T. L. Francavilla, and V. G. Harris, "(Ni,Fe,Co)-based nanocrystalline soft magnets with near-zero magnetostriction," *IEEE Trans. Magn.*, vol. 38, no. 5, pp. 3045–3050, Sep. 2002, doi: 10.1109/TMAG.2002.802435.

[17] M. A. Willard *et al.*, "Structure and magnetic properties of (Fe0.5Co0.5)88Zr7B4Cu1 nanocrystalline alloys," *J. Appl. Phys.*, vol. 84, no. 12, pp. 6773–6777, Dec. 1998, doi: 10.1063/1.369007.

[18] P. R. Ohodnicki, S. Y. Park, H. K. McWilliams, K. Ramos, D. E. Laughlin, and M. E. McHenry, "Phase evolution during crystallization of nanocomposite alloys with Co:Fe ratios in the two-phase region of the binary Fe-Co phase diagram," *J. Appl. Phys.*, vol. 101, no. 9, May 2007, doi: 10.1063/1.2711283.

[19] P. R. Ohodnicki, J. Long, D. Laughlin, M. McHenry, V. Keylin, and J. Huth, "Composition dependence of field induced anisotropy in ferromagnetic (Co,Fe)89Zr7B4 and (Co,Fe)88Zr7B4Cu1 amorphous and nanocrystalline ribbons," *J. Appl. Phys.*, vol. 104, pp. 113909–113909, Jan. 2009, doi: 10.1063/1.3021141.

[20] G. Herzer, "Modern soft magnets: Amorphous and nanocrystalline materials," *Acta Mater.*, vol. 61, no. 3, pp. 718–734, Feb. 2013, doi: 10.1016/j.actamat.2012.10.040.

[21] G. Herzer, "Nanocrystalline Soft Magnetic Alloys," in *Handbook of Magnetic Materials*, 1st ed., vol. 10, K. H. J. Buschow, Ed. Elsevier Science B.V., 1997, pp. 415–462. Accessed: Mar. 31, 2020. [Online]. Available: https://www.elsevier.com/books/handbook-of-magnetic-materials/buschow/978-0-444-82599-5

[22] Y. Han, Z. Wang, X. Che, X. Chen, W. Li, and Y. Li, "Influence of Co content on the structure and magnetic permeability of nanocrystalline (Fe1−xCox)73.5Cu1Nb3Si13.5B9 alloys," *Mater. Sci. Eng. B*, vol. 156, no. 1–3, pp. 57–61, Jan. 2009, doi: 10.1016/j.mseb.2008.11.006.

[23] G. Herzer, "Grain size dependence of coercivity and permeability in nanocrystalline ferromagnets," *IEEE Trans. Magn.*, vol. 26, no. 5, pp. 1397–1402, Sep. 1990, doi: 10.1109/20.104389.

[24] B. Hutchinson and J. Swift, "Anisotropy in Some Soft Magnetic Materials," *Texture*, vol. 1, Jan. 1972, doi: 10.1155/TSM.1.117.

[25] U. Köster, U. Schünemann, M. Blank-Bewersdorff, S. Brauer, M. Sutton, and G. B. Stephenson, "Nanocrystalline materials by crystallization of metal–metalloid glasses," in *Rapidly Quenched Materials*, H. Fredriksson and S. Savage, Eds. Oxford: Elsevier, 1991, pp. 611–615. doi: 10.1016/B978-0-444-89107-5.50148-9.

[26] K. Hono, A. Inoue, and T. Sakurai, "Atom probe analysis of Fe73.5Si13.5B9Nb3Cu1 nanocrystalline soft magnetic material," *Appl. Phys. Lett.*, vol. 58, no. 19, pp. 2180–2182, May 1991, doi: 10.1063/1.104968.

[27] K. Hono, K. Hiraga, Q. Wang, A. Inoue, and T. Sakurai, "The microstructure evolution of a Fe73.5Si13.5B9Nb3Cu1 nanocrystalline soft magnetic material," *Acta Metall. Mater.*, vol. 40, no. 9, pp. 2137–2147, Sep. 1992, doi: 10.1016/0956-7151(92)90131-W.

[28] Y. M. Chen, T. Ohkubo, M. Ohta, Y. Yoshizawa, and K. Hono, "Three-dimensional atom probe study of Fe–B-based nanocrystalline soft magnetic materials," *Acta Mater.*, vol. 57, no. 15, pp. 4463–4472, Sep. 2009, doi: 10.1016/j.actamat.2009.06.008.

[29] M. Ohnuma, D. H. Ping, T. Abe, H. Onodera, K. Hono, and Y. Yoshizawa, "Optimization of the microstructure and properties of Co-substituted Fe–Si–B–Nb–Cu nanocrystalline soft magnetic alloys," *J. Appl. Phys.*, vol. 93, no. 11, p. 9186, May 2003, doi: 10.1063/1.1569396.

[30] W. Guo, P.-P. Choi, and J.-B. Seol, "Amorphous phase separation in an Fe-based bulk metallic glass," *Mater. Lett.*, vol. 190, pp. 161–164, Mar. 2017, doi: 10.1016/j.matlet.2017.01.012.

[31] N. Mattern, A. Shariq, B. Schwarz, U. Vainio, and J. Eckert, "Structural and magnetic nanoclusters in Cu50Zr50−xGdx (x=5at.%) metallic glasses," *Acta Mater.*, vol. 60, no. 5, pp. 1946–1956, Mar. 2012, doi: 10.1016/j.actamat.2012.01.019.

[32] A. Shariq and N. Mattern, "A study of phase separated Ni66Nb17Y17 metallic glass using atom probe tomography," *Ultramicroscopy*, vol. 111, no. 8, pp. 1370–1374, Jul. 2011, doi: 10.1016/j.ultramic.2011.05.005.

[33] K. G. Pradeep, G. Herzer, P. Choi, and D. Raabe, “Atom probe tomography study of ultrahigh nanocrystallization rates in FeSiNbBCu soft magnetic amorphous alloys on rapid annealing,” *Acta Mater.*, vol. 68, pp. 295–309, Apr. 2014, doi: 10.1016/j.actamat.2014.01.031.

[34] Y. Nomura J. Uzuhashi, T. Tomita, T. Takahashi, H. Kuwata, T. Abe, T. Ohkubo, and K. Hono, “Heating rate dependence of coercivity and microstructure of Fe–B–P–Cu nanocrystalline soft magnetic materials,” *J. Alloys Compd.*, vol. 859, p. 157832, Apr. 2021, doi: 10.1016/j.jallcom.2020.157832.

[35] F. Betts, A. Bienenstock, D. T. Keating, and J. P. deNeufville, “Neutron and X-ray diffraction radial distribution studies of amorphous Ge0.17Te0.83,” *J. Non-Cryst. Solids*, vol. 7, no. 4, pp. 417–432, May 1972, doi: 10.1016/0022-3093(72)90276-1.

[36] T. Egami, “Structure of magnetic amorphous alloys studied by energy dispersive X-ray diffraction,” *J. Appl. Phys.*, vol. 50, no. B3, pp. 1564–1569, Mar. 1979, doi: 10.1063/1.327257.

[37] J. Chang and D. B. Dove, “Electron diffraction RDF analysis of amorphous As2Se3,AAs2Se2Te, As2SeTe2 and As2Te3 films,” *J. Non-Cryst. Solids*, vol. 16, no. 1, pp. 72–82, Oct. 1974, doi: 10.1016/0022-3093(74)90069-6.

[38] A.M.M Abeykoon, H. Hu, L. Wu, Y. Zhu, and S.J.L. Billinge, “Calibration and data collection protocols for reliable lattice parameter values in electron pair distribution function studies,” *J. Appl. Crystallogr.*, vol. 48, no. 1, pp. 244–251, 2015, doi: 10.1107/S1600576715000412.

[39] D. R. G. Mitchell and T. C. Petersen, “RDFTools: A software tool for quantifying short-range ordering in amorphous materials,” *Microsc. Res. Tech.*, vol. 75, no. 2, pp. 153–163, 2012, doi: 10.1002/jemt.21038.

[40] J. Shanmugam, K. B. Borisenko, Y.-J. Chou, and A. I. Kirkland, “eRDF Analyser: An interactive GUI for electron reduced density function analysis,” *SoftwareX*, vol. 6, pp. 185–192, Jan. 2017, doi: 10.1016/j.softx.2017.07.001.

[41] “ePDF Applications,” *Nanomegas*. https://nanomegas.com/literature/epdf-applications/ (accessed Apr. 22, 2022).

[42] H. E. Kissinger, “Variation of peak temperature with heating rate in differential thermal analysis,” *J. Res. Natl. Bur. Stand.*, vol. 57, no. 4, p. 217, Oct. 1956, doi: 10.6028/jres.057.026.

[43] D. Chen, X. Gao, and D. Dollimore, “A generalized form of the Kissinger equation,” *Thermochim. Acta*, vol. 215, pp. 109–117, Feb. 1993, doi: 10.1016/0040-6031(93)80085-O.

[44] T.-H. Chang and Y. Zhu, “A microelectromechanical system for thermomechanical testing of nanostructures,” *Appl. Phys. Lett.*, vol. 103, no. 26, p. 263114, Dec. 2013, doi: 10.1063/1.4858962.

[45] N. McCormick and J. Lord, “Digital Image Correlation,” *Mater. Today*, vol. 13, no. 12, pp. 52–54, Dec. 2010, doi: 10.1016/S1369-7021(10)70235-2.

[46] International Digital Image Correlation Society *et al.*, “A Good Practices Guide for Digital Image Correlation,” International Digital Image Correlation Society, Oct. 2018. doi: 10.32720/idics/gpg.ed1.

[47] A. Leary, V. Keylin, A. Devaraj, V. DeGeorge, P. Ohodnicki, and M. E. McHenry, “Stress induced anisotropy in Co-rich magnetic nanocomposites for inductive applications,” *J. Mater. Res.*, vol. 31, no. 20, pp. 3089–3107, Oct. 2016, doi: 10.1557/jmr.2016.324.

[48] A. Hernando and T. Kulik, “Exchange interactions through amorphous paramagnetic layers in ferromagnetic nanocrystals,” *Phys. Rev. B Condens. Matter*, vol. 49, no. 10, pp. 7064–7067, Mar. 1994, doi: 10.1103/physrevb.49.7064.

[49] H. Yun, X. Liu, T. Paik, D. Palanisamy, J. Kim, W.D. Vogel, A.J. Viescas, J. Chen, G.C. Papaefthymiou, J.M. Kikkawa, M.G. Allen, and C.B. Murray, “Size- and Composition-Dependent Radio Frequency Magnetic Permeability of Iron Oxide Nanocrystals,” Nov. 19, 2014. https://pubs.acs.org/doi/pdf/10.1021/nn504711g (accessed Apr. 06, 2020).

[50] K. Ohta, “Magnetocrystalline Anisotropy and Magnetic Permeability of Mn-Zn-Fe Ferrites,” *J. Phys. Soc. Jpn.*, vol. 18, no. 5, pp. 685–690, May 1963, doi: 10.1143/JPSJ.18.685.

CHAPTER 2: EVALUATING THE EFFECT OF MN COMPOSITION ON CHEMICAL PARTITIONING IN $CO_{(78-X)}FE_2MN_XB_{14}SI_2NB_4$ MAGNETIC AMORPHOUS NANOCOMPOSITES

Alicia G. Koenig[a], David Tweddle[a], Alex Leary[b], Ronald Noebe[b], Claudia Mewes[c], Tim Mewes[c], and Gregory B. Thompson[a]

[a] The University of Alabama, Department of Metallurgical & Materials Engineering, Box 870202 Tuscaloosa, AL 35473, USA

[b] NASA Glenn Research Center, Materials and Structures Division, Cleveland, Ohio 44135, USA

[c] The University of Alabama, Department of Physics & Astronomy, MINT Center, Tuscaloosa, AL 35473, USA

Published in Journal of Alloys and Compounds, 2021. DOI: 10.1016/j.jallcom.2021.159976

Abstract

We report the chemical partitioning behavior in a series of melt spun, partially crystallized $Co_{(78-x)}Fe_2Mn_xB_{14}Si_2Nb_4$ (x = 0.5, 2.0, 4.0, and 6.0) alloys. Upon annealing at 520°C anneal for 20 minutes, nanocrystallites precipitated from the amorphous matrix that have been previously reported to decrease the magnetic permeability with increasing Mn content. Transmission electron microscopy identified the crystallites within the continuous amorphous matrix as a mixture of hexagonal close packed and face centered cubic phases with an average size of 7.0 ± 3.0 nm. Atom probe tomography (APT) revealed an increase in chemical partitioning between the ferromagnetic and glass-forming elements upon annealing with the crystallite density increasing with Mn content. This implied an increase in crystallinity and a reduction of point defects (vacancies) that accompanied changes in Mn content during the

chemical partitioning process, where the extent of crystallinity would influence magnetic properties.

2.1 Introduction

The transformation, conversion, and storage of power occurs in nearly all electronic devices. Power efficiency is a direct function of the power losses that occur during these processes. These losses also generate heat, contributing to a limitation in minimum component size due to inadequate surface area for heat flux to occur [1], [2]. For these reasons, advancements in electric power conversion components through improvements in materials that deliver higher power-to-weight outputs in electric motors would facilitate the production of more efficient vehicles [3]. This will contribute to efforts to reduce reliance on fossil fuel driven power systems that create carbon emissions [4]. To that end, significant research has been directed towards increasing capabilities of soft magnetic materials to operate in high energy density environments [5]. Changes in alloy composition as well as processing of these soft magnetic materials can adjust the magnetic properties that minimize energy loss during field reversal in inductor and transformer cores [6].

Of these soft magnetic alloys, magnetic amorphous nanocomposites (MANCs) are a particularly promising class because of their scalable manufacturing, tunable magnetic properties, and favorable performance under medium to high frequency magnetic field reversal while maintaining low losses [7]. These alloys are typically rich in strongly ferromagnetic species, i.e., Fe and Co, while also containing a number of other alloying elements to stabilize the desired nanostructure. MANCs comprise nanocrystallites, typically < 20 nm, embedded within an amorphous matrix that forms an intergranular boundary separating the crystallites. This

amorphous matrix also provides for an increased resistivity while the nanoscale crystallites, whose average diameter is well below the ferromagnetic exchange length, exhibit low coercivity and variable permeability [8]. Within the broader random anisotropy model, intergranular distances [9], crystal structures and their textures [10], extent of crystallinity [11], as well as volume fractions and alignment of the relevant phases also contribute to these and other magnetic properties [12]–[15]. This gives MANCs great flexibility in achieving specific properties through alloy composition and subsequent processing to control the micro/nano-structure of these crystallites.

One such critical property in high frequency, alternating current applications is the magnetic permeability as it directly controls inductive properties. Of particular interest in such applications are materials that operate at high core temperatures enabling uses in engine-based applications [16]. Co-based alloys, because of their increased Curie temperature as compared to Fe-based alloys [17], are one such candidate alloy class. Recently, the MANC $Co_{(80-x-y)}Fe_xMn_yB_{14}Si_2Nb_4$ alloys received considerable interest because of its remarkable changes in magnetic permeability after stress annealing these alloys at temperatures of 520 °C [18]. This significant reduction in magnetic permeability, **Table 2.1**, has been attributed, in part, to planar defects formed in the nanocrystallites [19]. While a structural defect contribution has been identified, it was also found that the permeability was a strong function of Mn content, with the mechanisms for that particular chemical influence still elusive. Arguably, the difficulty in assessing the chemical contributions resides in characterizing the chemical partitioning in such fine scale, multi-component alloys.

Atom probe tomography (APT) has emerged as a technique well suited to characterizing the chemical structure for these types of materials [20], [21]. Its high chemical sensitivity and

atomic scale spatial resolution provides an ideal method for the detection and characterization of subtle changes in chemical positioning and behavior in nanoscale materials. This technique has successfully revealed the preferences of specific species to partition to either the crystalline or the amorphous phases in Co-based and similar MANCs, with such information being invaluable in understanding the compositional effects on magnetic properties. In this paper, we report the use of APT, along with transmission electron microscopy (TEM), to characterize the chemical partitioning and microstructure of the $Co_{(80-x-y)}Fe_xMn_yB_{14}Si_2Nb_4$ alloys under stress-free annealing conditions. The objective is to establish how the Mn content contributes to the partial crystallization and subsequent compositional partitioning behavior between the two phases.

Table 2.1 Permeability as a function of Mn content after stress annealing at 520 °C and 200 MPa, as reported via isopermeability plots in [18].

Sample ID (at.%)	$\mu_{relative}$ (H/m)
Mn = 0.5	~10,000
Mn = 2.0	~1,000
Mn = 4.0	~35
Mn = 6.0	~23

2.2 Materials and methods

A series $Co_{78-x}Fe_2Mn_xNb_4Si_2B_{14}$ ($0.5 \leq x \leq 6$) alloys were planar flow melt spun in air under a shielding atmosphere of Ar to produce amorphous ribbons that were 20 μm thick and approximately 3 mm in width using a large-scale, 5 kg planar flow caster built for the Magnetic Materials Lab at NASA Glenn Research Center. More details on the ribbon fabrication can be found in reference [22].

The samples were sectioned and subsequently encapsulated in a quartz ampule that was flushed twice with Ar, sealed, and annealed at 520°C for 20 minutes to partially crystallize the as-cast material, with the annealing temperature and time condition based on the prior work by Leary *et al.* [18]. The ampule was then removed from the furnace and allowed to cool to room temperature.

Both the as-cast and annealed ribbons were prepared for APT analysis via a focused ion beam (FIB) lift-out procedure [23]. Using a FEI Quanta 3D Dual Beam FIB/SEM and OmniProbe micromanipulator, a bar-shaped sample was milled from the 'shiny' side of the ribbon (the surface that was not in contact with the water-cooled cooper spinning wheel). The extracted wedge-shaped sample from each ribbon was attached to an array of silicon microtips and annular sharpened to approximately 70 nm in radius in a TESCAN LYRA FIB-FESEM creating the needle tip shape required for field evaporation. This annular milling was sequentially stepped down from 200 pA to 100 pA at 30 keV with a final ion beam setting of 5 keV and 30 pA to polish the tip which has been shown to reduce any potential damage from Ga^+ implantation [24]. The sharpened tips were then field evaporated in the CAMECA Local Electrode Atom Probe (LEAP) 5000XS, with a detector efficiency near 80%. The operating parameters of the LEAP consisted of a specimen set point of 40 K, laser pulse energy of 30 pJ, and pulse repetition rate of 625 kHz, with a per pulse detection rate of 0.5%.

The APT datasets were reconstructed using CAMECA's Integrated Visualization and Analysis Software (IVAS) 3.8.0. Two chemically distinct phases were observed, one being Co-rich (the crystallite phase) and the other being Co-lean (the amorphous phase). As the visualization and compositional analysis of these phases is dependent upon the method to delineate them, it can be difficult to consistently identify regions across different datasets using

either the same isoconcentration and/or isodensity values [25], [26]. In this work, as will be shortly shown, we found that isodensity delineation was the most effective means to identify and compare the nanocrystalline phases between the different annealed alloys. The isodensity values for each dataset were selected and subsequently refined by visually matching isosurface placement with atom maps in a procedure similar to that by Tang *et al*. [27].

The TEM samples were lifted out from the bulk ribbon using the same FEI Quanta 3D Dual Beam FIB/SEM and OmniProbe micromanipulator system described above. The specimens were mounted to a copper TEM half-grid and subsequently thinned to electron transparency via milling in the TESCAN LYRA FIB-FESEM with a final polish at a beam setting of 5 keV and 30 pA to remove Ga^+ damage as described previously. The samples were examined using an FEI Tecnai F-20 (S)TEM operated at 200 keV.

2.3 Results

A representative bright-field TEM micrograph of the 4 at.% Mn alloy (in the post annealed state) is shown in **Figure 2.1**. The microstructure consists of nanocrystallites with sizes < 10 nm encased within the amorphous matrix. Several high-resolution TEM (HRTEM) images were taken from multiple areas for this and all other annealed alloys with the measured grain sizes summarized in **Table 2.2**. With the extremely small grain sizes and a significant amorphous signal contribution, the selected area diffraction (SAD) patterns revealed notably broad and diffuse rings but whose reflections corresponded to the h-k=3N visibility criterion for the close packed structures, where the three index notation (hkl) is used for the HCP phase [19], [28]. Lattice fringe imaging of the crystallites, via a fast Fourier transforms (FFTs) taken of the HRTEM micrographs, were also generated revealing additional inter-planar spacings that were

not strongly diffracting in the SAD patterns [29]. The resulting FFTs consistently revealed periodicities with unique d-spacings found for the hexagonal close packed (HCP) Co phase as well as the face centered cubic (FCC) Co phase within the individual crystallites sampled [30], [31]. While it is not practical to sample every crystallite, we captured tens of crystallites in all alloys whereupon a mix HCP and FCC FFT patterns were observed in each alloy. A representative example is shown for regions A and B in **Figure 2.1**, with the distinguishing inter-planar spacing bolded in the table inset in **Figure 2.1**. As the SAD patterns and FFT findings were consistent for all other alloys in the series, with no clear and observable differences between different Mn concentrations, the 4 at.% Mn alloy in **Figure 2.1** is provide as the representative set of images for the series.

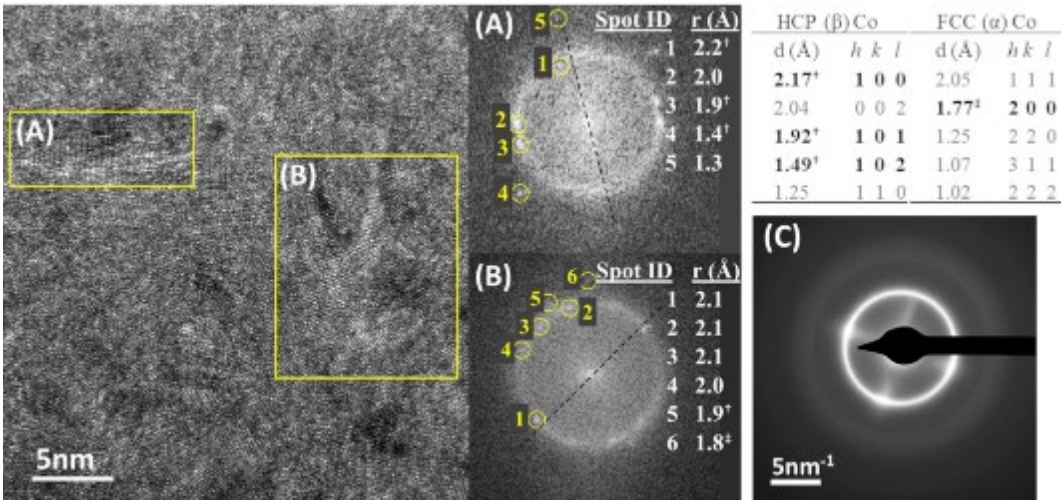

Figure 2.1 HRTEM of $Co_{74}Fe_2Mn_4Nb_4Si_2B_{14}$, post-anneal, and FFT for each of the indicated regions. The (A) and (B) FFT patterns are from the same identified region in the alloy with a table of the measured spacing to ring numbers provided. Measurements show that the areas of increased periodicity consistent with both FCC and HCP d-spacings. (C) The selected area diffraction pattern. † *Distinct to HCP* ‡ *Distinct to FCC*

Table 2.2 Grain size as estimated from BF TEM imaging

Sample ID	D_{grain} (nm)
Mn = 0.5	6.5 ± 2.2
Mn = 2.0	7.6 ± 3.6
Mn = 4.0	6.8 ± 2.8
Mn = 6.0	7.0 ± 2.6

Table 2.3 tabulates the composition between the targeted alloy, the overall measurement for each alloy (B for bulk), and the two phases within the sample (with C for crystallite and M for matrix, which is the amorphous phase). The bulk compositions largely agreed with expected target values, except for a lower APT measurement of the B content. This difference is attributed to the field evaporation behavior of B, which often generates a larger number of multi-hit events that leads to a chronic underrepresentation of the B signal in the mass spectrum [32], [33].

Table 2.3 Bulk (B), nanocrystalline (C), and amorphous matrix (M) compositions as measured by APT (at.%).

	Mn = 0.5 at.%			Mn = 2.0 at.%			Mn = 4.0 at.%			Mn = 6.0 at.%			**Nominal**	
	Bulk	C	M	**Bulk**	C	M	**Bulk**	C	M	**Bulk**	C	M		
B	7.3	3.8	7.8	8.1	4.8	8.5	7.2	3.1	7.7	7.7	2.9	8.2	14.0	
Co	81.6	87.5	80.7	78.4	84.6	77.6	77.6	87.3	76.4	74.5	86.0	73.2	77.5, 74.0,	76.0, 72.0
Nb	5.0	3.7	5.2	5.5	4.0	5.6	5.3	2.5	5.6	5.3	2.6	5.5	4.0	
Si	2.2	1.4	2.3	2.2	1.4	2.3	2.1	0.7	2.2	2.0	0.7	2.2	2.0	
Fe	2.5	2.6	2.5	2.6	2.9	2.5	2.9	4.2	2.7	3.1	4.4	2.9	2.0	
Mn	0.6	0.5	0.6	2.2	1.6	2.2	4.7	2.1	5.0	6.6	3.0	7.0	0.5, 4.0,	2.0, 6.0
(other)	0.8	0.5	0.9	1.0	0.7	1.2	0.2	0.1	0.3	0.8	0.4	1.0	-	

In references [18], [22], a similar alloy $Co_{75.4}Fe_{2.3}Mn_{2.3}Nb_4Si_2B_{14}$ alloy was characterized by APT where upon it was shown to partition into two main components - a Co-rich region that

was the crystalline phase and a Co-lean amorphous region (matrix). By comparing the bulk, crystallite, and matrix compositions, we confirm that Fe tends to partition to the Co-rich crystallites while the other elements prefer the B-rich matrix. **Figure 2.2(a)** are a series of high-density Co-rich regions extracted by isodensity surfaces. These regions appear randomly distributed throughout the amorphous matrix with these regions becoming (qualitatively) more distinct with increasing Mn concentration. The sizes of these features are consistent with TEM observations for the crystallite phases as shown in **Figure 2.1**. In **Figure 2.2(b)**, which is a representative APT 2D density contour map taken from each alloy, reveals evidence that the density of the crystallites increases with Mn content.

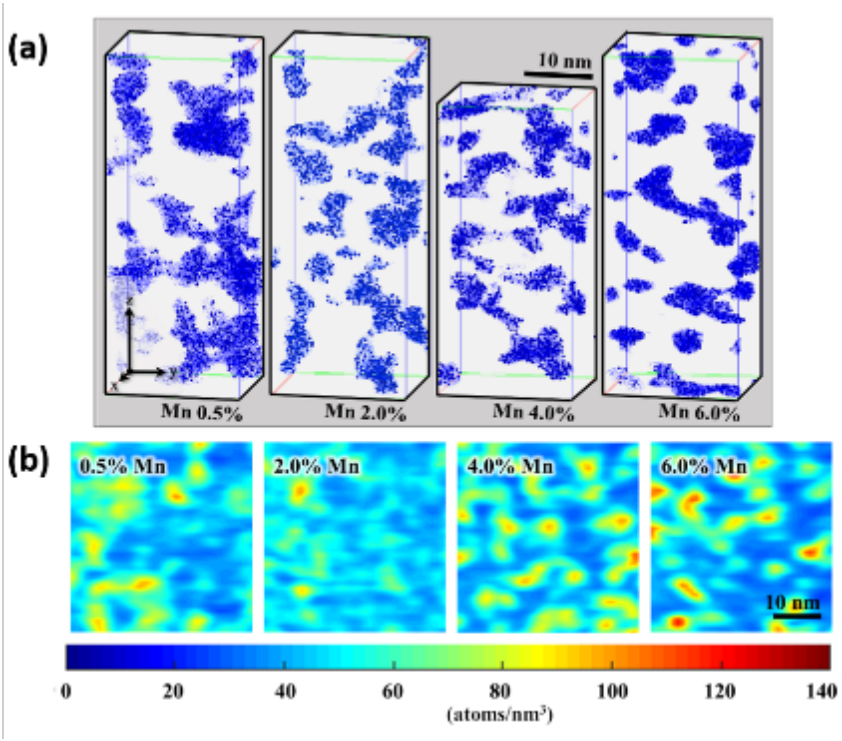

Figure 2.2 (a) Nanocrystalline regions as defined by isodensity surfaces for each alloy in the series. The isodensity values used to define the surfaces were ρ = 68.8, 62.4, 78.7, 84.0 ions/nm^3 for Mn = 0.5, 2, 4, 6, respectively, following the method outlined in Tang *et al.* [27]. (b) 2D density maps for each $Co_{78-x}Fe_2Mn_xNb_4Si_2B_{14}$ sample. Densities are in atoms/nm^3 and have been corrected for detector efficiency.

Table 2.4 summarizes the bulk tip and secondary crystallite density for each of the alloys. The crystallite density quantitatively shows a statistically significant difference in the reconstructed densities for this phase between the different Mn containing alloys, which agrees with the visual observations shown in **Figure 2.2(b)**. Here, the error is given by the differences from the average densities between each crystallite phase. As an atom probe reconstruction is sensitive to the input values of image compression factor, shank angle, etc. [25] that are used in the reconstruction, we have also included in **Table 2.4** the overall bulk density from the reconstructed tip. These values and errors were provided by taking segmented regions of interest throughout the reconstructed volume of the tip and averaging those values with the standard error between each value. While all the tips were annular milled to be as similar as possible, inevitable variations will exist and contribute to some modest changes in the reconstruction parameters. Nevertheless, we found that the same reconstruction parameters were appropriate between all the reconstructions with the bulk densities being statistically equivalent to each other for all Mn contents. This gives us confidence that use of the equivalent reconstruction parameters were not only appropriate but that the crystallite phase's density changes were a result in an increase in crystallinity for this phase.

Table 2.4 Calculated bulk and nanocrystalline phase densities for each alloy. The bulk densities were calculated as an average of those measured in several 10x10x10 nm cubic regions of interest taken within the analyzed tip volume. The crystallite densities were calculated as an average of sampled densities of the 8 largest (by volume) isodensity surfaces.

Sample ID	ρ *(atoms/nm3)*	
	Bulk	Crystallite
Mn = 0.5	63 ± 5	90 ± 2
Mn = 2.0	55 ± 3	78 ± 8
Mn = 4.0	58 ± 5	115 ± 2

Mn = 6.0	57 ± 6	125 ± 3

Finally, we comment that the values tabulated in **Table 2.4** are used as a measure of a trend and not specifically the absolute value of density. Even though we have used the same reconstruction parameters across all samples, this does not mitigate inherent limitations in APT reconstructions including detector efficiency in collecting all of the atoms [34] and image compression outcomes when reconstructing the atoms into their spatial positions based upon the single field evaporation method [35], [36]. The single evaporation field approximation assumes the same field strength is required to evaporate each atom in the tip, independent of phase. Thus, in a multi-phase system, this can create local variation in densities if differences in evaporation strengths exist between each phase [37]. When a reconstructed region (phase) has a higher evaporation field strength, those atoms are spatially widened from each other because it is assuming a larger reconstructed radius creating a less dense region. In contrast, if the region has a lower field than the approximation, the reconstructed radius is smaller creating a localized increase in the density of atoms [38]. Since both phases co-exist in the tip, reconstruction of the tip is based on a 'best estimate' balance between these factors. For that reason, the use of the equivalent reconstruction parameters across all Mn contents above enables us to conclude that the relative trend observed in the crystallite phases with Mn content is appropriate, even though the absolute density value itself may be incorrect. For example, HCP Co has near 91 atoms/nm^3 but in some of the crystallites, **Figure 2.2(b)**, there are density measurements approaching 120 atoms/nm^3 in the core of the crystallites created by the aforementioned reconstruction artifact.

Table 2.5 is a tabulation of the morphological characteristics of the crystallite phase within the amorphous matrix. The number density, ρ_{number}, was determined by counting the number of crystallite regions found, n, and dividing it by the volume of the dataset, V_T, i.e.,

$\rho_{number} = n/V_T$. From these values, the average spacing between crystallites was calculated using the assumptions described in [39]. With increasing Mn content, the number density of crystallites increased while the diameters of the crystallites remain relatively equivalent, considering the standard deviation error.

Table 2.5 The calculated number density ρ_{number}, average diameter $d_{crystallite}$, and average intercrystallite spacing $<R_a>$, of the precipitates as defined by isodensity surfaces.

Sample ID	ρ_{number} (crystallites/m^3)	$d_{crystallite}$ (nm)	$<R_a>$ (nm)
Mn = 0.5	3.3 E+23	4.8 ± 1.1	4.0
Mn = 2.0	5.5 E+23	4.7 ± 1.1	4.1
Mn = 4.0	6.3 E+23	4.7 ± 1.1	4.2
Mn = 6.0	7.1 E+23	4.5 ± 0.8	4.2

Figure 2.3 displays the isodensity surface-based proximity histograms (proxigrams) that reveals the average concentration profile originating from the collective average from all of the defined isodensity interfaces in **Figure 2.2(a)**. From this figure a number of observations are drawn. First, the increased partitioning with increasing Mn content is obvious in elements that segregate to the high-density, crystallite region, i.e., Fe and Co. Particularly striking is the Co content, which remains relatively invariant in its composition in the crystallite phase, though it is reduced in the bulk alloy at the expense of the Mn increase. This may explain why its compositional depletion becomes more pronounced in the matrix with increasing Mn. In contrast, the Fe content reveals a near doubling of its concentration into the crystallite phase with increasing Mn content.

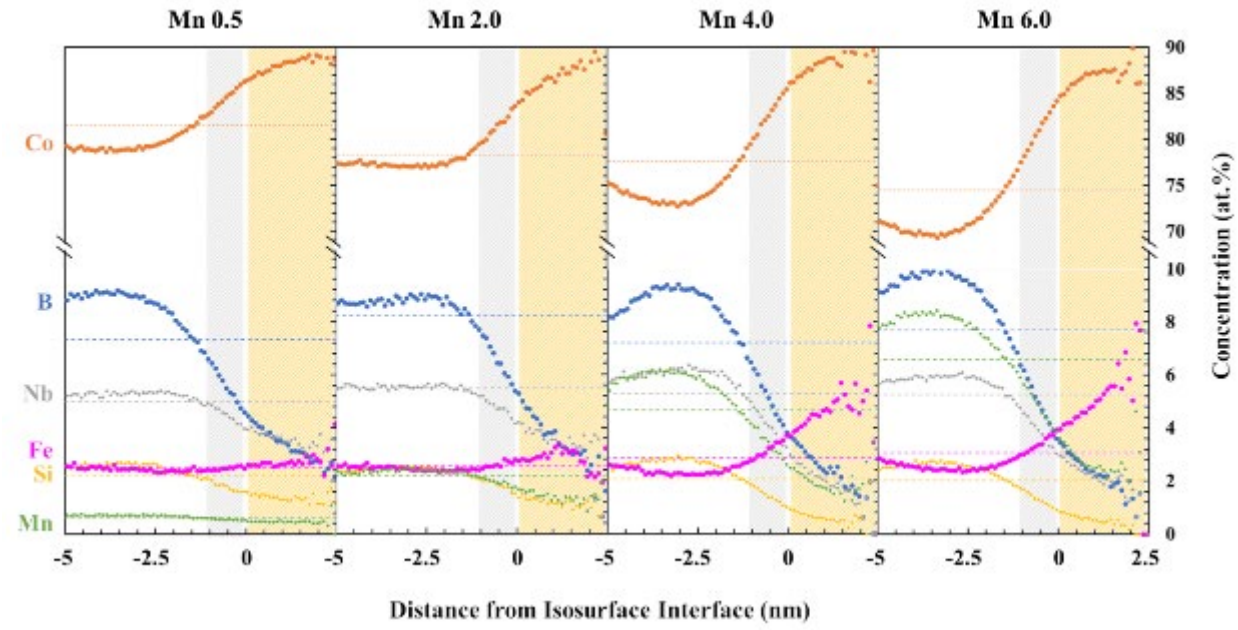

Figure 2.3 Proxigrams from each alloy in the $Co_{78-x}Fe_2Mn_xNb_4Si_2B_{14}$ series. The orange region marks the upper-bounded region of the isodensity surface, i.e. the crystallites. The grey region defines the location of the interphase region between the crystalline and amorphous phases.

Correspondingly, the glass forming elements being B and Si are enriched in the matrix amorphous region and exhibit a clear depletion from the high-density Co-rich region. The expulsion of these elements from the crystallites creates a broad interphase region between the Co-rich and Co-lean regions as well. The average inter-crystallite spacing is on the order of 4 nm, **Table 2.5**, with the proxigrams revealing the depletion of Co and Fe and enrichment of Si and B span a similar length-scale. The early transition metal, Nb, revealed a very slight rise in composition within the matrix phase with increasing Mn content. This behavior is consistent with previous findings in other alloy systems [40], [41], and illustrates Nb's hindrance of grain growth as discussed in [42]. Finally, we note that Mn, with its increasing content, replicates the concentration profile observed for B.

2.4 Discussion

The representative TEM micrograph of the microstructure, included in **Figure 2.1**, confirmed the presence of nanoscale crystallites in an amorphous matrix, with this type of microstructure common to all Mn compositions in the annealed condition. HRTEM micrographs showed the presence of HCP and FCC crystal structures within this phase. The presence of both phases is not necessarily surprising as they are close packed structures that only differ by a Shockley partial dislocation slip in their close packed plane arrangement. Furthermore, at elevated temperatures, Co undergoes an allotropic HCP to FCC phase change and in doing so is able to form a solid solution with Fe. While at lower temperatures, where Co is HCP, it has very limited solution with Fe (less than ~1 at.%) [43].

Since the Fe content in the crystallites is near 6 at.%, **Figure 2.3**, and well beyond Co's HCP thermodynamic solubility, it is not surprising that faulting consistent between HCP and FCC has occurred. Here, the Fe solutes likely are reducing the stacking fault energy and promoting a FCC stacking sequence [44], [45]. Additionally, the small size of the crystallites can influence the stability of both FCC and HCP ordering in nanocrystalline Co [46].

The faulting creates planar defects have been used to explain the significantly lower permeability in these alloys [18], albeit those alloys were pulled in tension during the annealing to promote planar faulting. Previous work has shown that deformation induced planar defects will indeed influence various magnetic properties, including magnetocrystalline anisotropy, in close packed Co-rich materials [47]. In this study, our alloys were annealed in a 'stress-free' condition demonstrating that this faulting still occurs, even without deformation. Thus, the presence of Fe likely facilitates more faulting of the Co nanocrystallites under loading by

reducing the stacking fault energy, where the concentration of Fe in the nanocrystallites was highest for the 4 at.% and 6 at.% Mn alloys.

Further, because these faults occurred without the application of stress, we believe these defects are growth-induced faulting. The presence of such faults has been suggested to modify local magnetic anisotropy fields [18]. The advantage of strain annealing is suspected to increase the density of these fault more than growth-based fault, but more work is still needed to verify these ideas. In the report by Leary et al. [18], which again are the same compositional alloys of our study here on partitioning, deformation induced faulting would be prevalent since they were strain annealed.

To understand the influence of Mn on the chemical partitioning, we note the increase in crystallite number density with Mn content, **Table 2.5**. This would suggest that the nucleation density is influenced by Mn content since all other processing conditions were the same. The nucleation thermodynamic considerations nominally involve the interfacial energy, strain energy, and volumetric free energy in the precipitation of a secondary phase [48]. An interfacial energy change, associated with structural consideration, is not likely a consideration change with Mn content since the crystallite phase precipitates out of an amorphous matrix, where no preferential interfaces would exist. This would also support that any strain energy considerations would be minimal (or non-existent); again, because the secondary phase precipitates in an amorphous alloy where no coherency issues would be present. While the interfacial structural (as well as strain energy) contributions are discounted, the chemical contribution to the interfacial energies could be present. However, a review of **Figure 2.3**'s proxigrams do not reveal any specific species enriching the interface between the two phases. This would suggest that the chemical considerations to the interfacial energy differences are rather similar between all alloys. Finally,

the volumetric free energy that drives precipitation could be altered by changes in composition. We return to the proxigrams in **Figure 2.3** and observe no notable differences in the type of chemical species in the crystalline phases. Rather, we observe an increase in Fe content, number density, and crystalline density (**Table 2.4**). While changes in composition can alter the absolute driving force values, the Fe in solution with Co suggest that any increases are minimal. Rather the change in crystallinity and number density suggest that a kinetic mechanism is more likely facilitating the nucleation increase with Mn content.

In the work by Belashchenko et al. [49], it was reported that higher B:Co ratios promotes a higher vacancy-like cavity formation in amorphous Co-B alloys, which would be a kinetic mechanism for increasing mass transport for diffusion since all the alloys were annealed under the same conditions. In our alloy, as the Mn is increased, it was done so at the expense of the Co, thereby increasing the relative B:Co ratio in our alloys. Though our alloys are far more compositionally complex than those reported by Belashchenko et al. [49], the relative shift in B:Co created by Mn may provide an explanation to a mechanism (i.e. vacancy-like free volume regions) that could increase the partitioning of the ferromagnetic elements into the crystalline phase. Density changes occurring in the crystalline regions are associated with the creation or removal of point defects in the crystalline lattice i.e. vacancies, whereas density changes occurring in amorphous regions are associated with changes in the amount of free volume [50], [51]. These regions of free volume may act as sources and sinks for vacancies in crystalline regions, and are likely responsible for the increased diffusion that is indicated by the increase in chemical partitioning. This diffusion would result in a corresponding reduction of vacancy point defects in the same crystallite phase as such defects must diffuse out and the ferromagnetic elements diffuse into the crystallite through an exchange mechanism.

This type of mass transport is supported by the relative changes in the Co and Fe compositional profiles between the 0.5 and 2 at.% and the 4 and 6 at.% Mn in **Figure 2.3**. The depletion (or dip) for Co and Fe is most prominent in the amorphous matrix at the higher Mn contents. To more readily mass transfer these elements from the amorphous phase into the crystallite phase, a higher concentration of free volumes must be present. Such an increase in free volume appears to be most effective in the mass transport of Fe into the crystallite phase, as it doubles its concentration in this phase between 4 at.% and 6 at.% Mn. In contrast, the Co concentration remained relatively the same over the same Mn compositional range, **Figure 2.3**. With this ferromagnetic species diffusion into the crystallite, with the corresponding exchange mechanism of vacancies out of the crystallite, we note that the core of the crystallites has the highest relative density, **Figure 2.2(b)**, which would be expected if such a mechanism was active. While an increase in Fe solute could also influence the atom probe reconstruction, Fe is in solution with Co suggesting that any such contribution is likely to be a secondary consideration to any such density artifacts. Thus, it appears that Mn facilities a mobility mechanism that consequently increases the crystallinity of the crystallite phase that contributes alongside the planar defects to the magnetic property changes reported in this alloy series.

This increase in free volume content with higher B:Co or, alternatively, Mn content, would also contribute to a higher nucleation rate of the crystallites, explaining the higher number density, **Table 2.5**. Furthermore, if the mass transport at higher Mn concentrations is increased because of this higher vacancy concentration, one could also expect an increased crystallite growth too. However, this exchange mechanism appears most dominate in the early stages of clustering and nucleation. To understand why the growth is limited after nucleation, we revisit the proxigrams of **Figure 2.3**. Here we note that the Nb content has increased within the

amorphous phase at these higher Mn contents. The early transition metals, like Nb, are added to MANCs to hinder crystallite coarsening [42]. Thus, with Nb's increase in the amorphous matrix, it is contributing to slowing down the coarsening kinetics. Furthermore, at the higher Mn contents, less Co and Fe now remains in the amorphous phase (evident by the prior discussion above regarding their concentration dips in this phase) leaving higher concentrations of B and Si in the matrix, which are the glass formers. Thus, one can consider that the amorphous phase is expelling species that could reduce its glass transition temperature, or alternatively, the partitioning is increasing the metastability of the amorphous phase. Finally, the open structure of an amorphous phase more readily absorbs the vacancies as free volume regions reducing their influence on diffusion as compared to a close packed crystalline structure. While one mechanism alone is likely insufficient to describe the complex chemical structure evolution, the APT results have provided new discernments between the elemental evolution as a function of Mn content.

2.5 Conclusion

In this paper, TEM and APT characterization was employed to study the structural and chemical evolution for a series of $Co_{(78-x)}Fe_2Mn_xB_{14}Si_2Nb_4$ alloys (x = 0.5, 2.0, 4.0, and 6.0 at.%). It was found that after a 20-minute static anneal at 520°C, partial crystallization occurred with average crystallite size of ~ 7 nm. The crystallites' structure was identified as a mix of HCP and FCC for all Mn composition alloys.

APT compositional analysis revealed a preference for Fe and Co to be in the crystalline phase, while B, Si, and Nb enriched the amorphous phase. The presence of solid solution of Fe in Co likely facilitated the presence of planar faulting that resulted in the mix HCP and FCC phases in the crystallites. At the higher Mn contents (4 and 6 at. %), notable increases in the APT

reconstructed densities of the crystallites were measured. This increase in crystallinity was explained by a potential increase in the vacancy point defect concentration associated with the B:Co ratio within the alloys. As the ferromagnetic species diffused into the crystallite via an exchange mechanism that has the vacancies leaving this phase, the crystallinity increased.

The collective APT (with TEM) characterization has provided distinct insights into how Mn concentration alters the compositional evolution between phases. It appears Mn facilitates mobility mechanisms which consequently influences the chemical partitioning. With species preferences to specific phases and their corresponding consequences on structural defects, such as mix phases via stacking faults in the crystallite phase as well as the extent of crystallinity in such phases, the insights necessary to understand structure-magnetic property outcomes within this class of magnetic amorphous nanocomposite is being revealed.

Acknowledgements

This work was supported by NASA CAN 80NSSC18M0023. Further, we would like to acknowledge the University of Alabama Analytical Research Center and staff. Additional support for this work came from the NASA Advanced Air Transport Technology Project, Electrified Aircraft Powertrain Technologies Subproject. R.D.N and A.M.L also acknowledge useful discussions and experimental support from V. Keylin, G. Feichter, and R. Bowman.

References

[1] S. Shen, P. Ohodnicki, S. Kernion, A. Leary, V. Keylin, J. Huth, and M.E. McHenry, "Nanocomposite Alloy Design for High Frequency Power Conversion Applications," in *Energy Technology 2012*, John Wiley & Sons, Ltd, 2012, pp. 265–274.

[2] A. M. Leary, P. R. Ohodnicki, and M. E. McHenry, "Soft Magnetic Materials in High-Frequency, High-Power Conversion Applications," *JOM*, vol. 64, no. 7, pp. 772–781, Jul. 2012, doi: 10.1007/s11837-012-0350-0.

[3] A. W. Lotfi and M. A. Wilkowski, "Issues and advances in high-frequency magnetics for switching power supplies," *Proc. IEEE*, vol. 89, no. 6, pp. 833–845, Jun. 2001, doi: 10.1109/5.931473.

[4] V. Madonna, P. Giangrande, and M. Galea, "Electrical Power Generation in Aircraft: Review, Challenges, and Opportunities," *IEEE Trans. Transp. Electrification*, vol. 4, no. 3, pp. 646–659, Sep. 2018, doi: 10.1109/TTE.2018.2834142.

[5] G. E. Fish, "Soft magnetic materials," *Proc. IEEE*, vol. 78, no. 6, pp. 947–972, Jun. 1990, doi: 10.1109/5.56909.

[6] J. M. Silveyra, E. Ferrara, D. L. Huber, and T. C. Monson, "Soft magnetic materials for a sustainable and electrified world," *Science*, vol. 362, no. 6413, Oct. 2018, doi: 10.1126/science.aao0195.

[7] M. A. Bahmani, T. Thiringer, and M. Kharezy, "Design Methodology and Optimization of a Medium-Frequency Transformer for High-Power DC–DC Applications," *IEEE Trans. Ind. Appl.*, vol. 52, no. 5, pp. 4225–4233, Sep. 2016, doi: 10.1109/TIA.2016.2582825.

[8] G. Herzer, "Grain size dependence of coercivity and permeability in nanocrystalline ferromagnets," *IEEE Trans. Magn.*, vol. 26, no. 5, pp. 1397–1402, Sep. 1990, doi: 10.1109/20.104389.

[9] A. Hernando and T. Kulik, "Exchange interactions through amorphous paramagnetic layers in ferromagnetic nanocrystals," *Phys. Rev. B Condens. Matter*, vol. 49, no. 10, pp. 7064–7067, Mar. 1994, doi: 10.1103/physrevb.49.7064.

[10] G. Herzer, "Nanocrystalline Soft Magnetic Alloys," in *Handbook of Magnetic Materials*, 1st ed., vol. 10, K. H. J. Buschow, Ed. Elsevier Science B.V., 1997, pp. 415–462.

[11] M. Zhu, Y. Fa, L. Yao, P. Tao, Z. Jian, and F. Chang, "The Influence of Annealing on the Structural and Soft Magnetic Properties of (Fe0.4Co0.6)79Nb3B18 Nanocrystalline Alloys," *Materials*, vol. 11, no. 11, Nov. 2018, doi: 10.3390/ma11112171.

[12] M. Ohnuma, D. H. Ping, T. Abe, H. Onodera, K. Hono, and Y. Yoshizawa, "Optimization of the microstructure and properties of Co-substituted Fe–Si–B–Nb–Cu nanocrystalline soft magnetic alloys," *J. Appl. Phys.*, vol. 93, no. 11, p. 9186, May 2003, doi: 10.1063/1.1569396.

[13] H. Yun, X. Liu, T. Paik, D. Palanisamy, J. Kim, W.D. Vogel, A.J. Viescas, J. Chen, G.C. Papaefthymiou, J.M. Kikkawa, M.G. Allen, and C.B. Murray, "Size- and Composition-Dependent Radio Frequency Magnetic Permeability of Iron Oxide Nanocrystals," Nov. 19, 2014. https://pubs.acs.org/doi/pdf/10.1021/nn504711g (accessed Apr. 06, 2020).

[14] K. Ohta, "Magnetocrystalline Anisotropy and Magnetic Permeability of Mn-Zn-Fe Ferrites," *J. Phys. Soc. Jpn.*, vol. 18, no. 5, pp. 685–690, May 1963, doi: 10.1143/JPSJ.18.685.

[15] J. Hwang, H. Lee, and S. Yi, "Formation and Magnetic Properties of Nanocomposites in Rapidly Solidified Fe42Ni41.7C7Si4.5B3.9P0.9 (at%) Ribbons," *Met. Mater. Int.*, vol. 25, pp. 1–8, Jan. 2019, doi: 10.1007/s12540-018-0163-y.

[16] C. L. Bowman, "Design Issues for Using Magnetic Materials in Radiation Environments at Elevated Temperature," p. 8, 2013.

[17] P. R. Ohodnicki, J. Long, D. Laughlin, M. McHenry, V. Keylin, and J. Huth, "Composition dependence of field induced anisotropy in ferromagnetic (Co,Fe)89Zr7B4 and (Co,Fe)88Zr7B4Cu1 amorphous and nanocrystalline ribbons," *J. Appl. Phys.*, vol. 104, pp. 113909–113909, Jan. 2009, doi: 10.1063/1.3021141.

[18] A. Leary, V. Keylin, A. Devaraj, V. DeGeorge, P. Ohodnicki, and M. E. McHenry, "Stress induced anisotropy in Co-rich magnetic nanocomposites for inductive applications," *J. Mater. Res.*, vol. 31, no. 20, pp. 3089–3107, Oct. 2016, doi: 10.1557/jmr.2016.324.

[19] A. M. Leary, V. Keylin, P. R. Ohodnicki, and M. E. McHenry, "Stress induced anisotropy in CoFeMn soft magnetic nanocomposites," *J. Appl. Phys.*, vol. 117, no. 17, p. 17A338, May 2015, doi: 10.1063/1.4919230.

[20] E. A. Marquis and J. M. Hyde, "Applications of atom-probe tomography to the characterisation of solute behaviours," *Mater. Sci. Eng. R Rep.*, vol. 69, no. 4–5, pp. 37–62, Jul. 2010, doi: 10.1016/j.mser.2010.05.001.

[21] K. Hono, Y. Zhang, A. Inoue, and T. Sakurai, "Atom Probe Studies of Nanocrystalline Microstructural Evolution in Some Amorphous Alloys," *Mater. Trans. JIM*, vol. 36, no. 7, pp. 909–917, 1995, doi: 10.2320/matertrans1989.36.909.

[22] A. Leary, "Mechanical Processing of Soft Magnetic Nanocomposites," Ph.D. Materials Science and Engineering, Carnegie Mellon University, Pittsburgh, PA, 2016.

[23] K. Thompson, D. Lawrence, D. J. Larson, J. D. Olson, T. F. Kelly, and B. Gorman, "In situ site-specific specimen preparation for atom probe tomography," *Ultramicroscopy*, vol. 107, no. 2–3, pp. 131–139, Mar. 2007, doi: 10.1016/j.ultramic.2006.06.008.

[24] P. J. Felfer, T. Alam, S. P. Ringer, and J. M. Cairney, “A reproducible method for damage-free site-specific preparation of atom probe tips from interfaces,” *Microsc. Res. Tech.*, vol. 75, no. 4, pp. 484–491, Apr. 2012, doi: 10.1002/jemt.21081.

[25] B. Gault, M. P. Moody, J. M. Cairney, and S. P. Ringer, *Atom Probe Microscopy*. New York: Springer-Verlag, 2012.

[26] B. C. Hornbuckle, M. Kapoor, and G. B. Thompson, “A procedure to create isoconcentration surfaces in low-chemical-partitioning, high-solute alloys,” *Ultramicroscopy*, vol. 159, pp. 346–353, Dec. 2015, doi: 10.1016/j.ultramic.2015.03.003.

[27] F. Tang, T. Alam, M. Moody, B. Gault, and J. Cairney, “Challenges Associated with the Characterisation of Nanocrystalline Materials Using Atom Probe Tomography,” *Mater. Sci. Forum*, vol. 654–656, Jun. 2010, doi: 10.4028/www.scientific.net/MSF.654-656.2366.

[28] B. E. Warren, *X-Ray Diffraction*. New York: Dover, 1969.

[29] “FFT Measurements.” https://imagej.nih.gov/ij/docs/examples/tem/ (accessed Mar. 26, 2020).

[30] “PDF-00-015-0806 (α-Co).” International Centre for Diffraction Data, 2018.

[31] “PDF-01-089-4308 (β-Co).” International Centre for Diffraction Data, 2020.

[32] F. Meisenkothen, E. B. Steel, T. J. Prosa, K. T. Henry, and R. Prakash Kolli, “Effects of detector dead-time on quantitative analyses involving boron and multi-hit detection events in atom probe tomography,” *Ultramicroscopy*, vol. 159, no. Part 1, pp. 101–111, Dec. 2015, doi: 10.1016/j.ultramic.2015.07.009.

[33] Y. Tu *et al.*, “Influence of laser power on atom probe tomographic analysis of boron distribution in silicon,” *Ultramicroscopy*, vol. 173, no. Supplement C, pp. 58–63, Feb. 2017, doi: 10.1016/j.ultramic.2016.11.023.

[34] “CAMECA LEAP 5000 Atom Probe.” https://www.cameca.com/products/apt/leap-5000 (accessed Apr. 22, 2020).

[35] M. P. Moody *et al.*, “Lattice Rectification in Atom Probe Tomography: Toward True Three-Dimensional Atomic Microscopy,” *Microsc. Microanal.*, vol. 17, no. 2, pp. 226–239, Apr. 2011, doi: 10.1017/S1431927610094535.

[36] B. Gault *et al.*, “A nexus between 3D atomistic data hybrids derived from atom probe microscopy and computational materials science: A new analysis of solute clustering in Al-alloys,” *Scr. Mater.*, vol. 131, pp. 93–97, Apr. 2017, doi: 10.1016/j.scriptamat.2017.01.011.

[37] X. Zhou and G. B. Thompson, “Charge-State Field Evaporation Behavior in Cu(V) Nanocrystalline Alloys,” *Microsc. Microanal.*, vol. 25, no. 2, pp. 501–510, Apr. 2019, doi: 10.1017/S1431927618016288.

[38] V. Radmilovic, A. Tolley, E. A. Marquis, M. D. Rossell, Z. Lee, and U. Dahmen, "Monodisperse Al3(LiScZr) core/shell precipitates in Al alloys," *Scr. Mater.*, vol. 58, no. 7, pp. 529–532, Apr. 2008, doi: 10.1016/j.scriptamat.2007.11.012.

[39] P. P. Bansal and A. J. Ardell, "Average nearest-neighbor distances between uniformly distributed finite particles," *Metallography*, vol. 5, no. 2, pp. 97–111, Apr. 1972, doi: 10.1016/0026-0800(72)90048-1.

[40] R. V. Ramanujan and Y. R. Zhang, "Quantitative transmission electron microscopy analysis of the nanocrystallization kinetics of soft magnetic alloys," *Phys. Rev. B*, vol. 74, no. 22, p. 224408, Dec. 2006, doi: 10.1103/PhysRevB.74.224408.

[41] C. Smith *et al.*, "Comparison of the Crystallization Behavior of Fe-Si-B-Cu and Fe-Si-B-Cu-Nb-Based Amorphous Soft Magnetic Alloys," *Metall. Mater. Trans. A*, vol. 45, no. 7, pp. 2998–3009, Jun. 2014, doi: 10.1007/s11661-014-2239-8.

[42] M. McHenry, F. Johnson, H. Okumura, T. Ohkubo, V. Ramanan, and D. Laughlin, "The kinetics of nanocrystallization and microstructural observations in FINEMET, NANOPERM and HITPERM nanocomposite magnetic materials," *Scr. Mater. - Scr. MATER*, vol. 48, Apr. 2003, doi: 10.1016/S1359-6462(02)00597-3.

[43] H. Okamoto, "Co-Fe (Cobalt-Iron)," *J. Phase Equilibria Diffus.*, vol. 29, no. 4, pp. 383–384, Aug. 2008, doi: 10.1007/s11669-008-9345-5.

[44] K. Edalati *et al.*, "Influence of dislocation–solute atom interactions and stacking fault energy on grain size of single-phase alloys after severe plastic deformation using high-pressure torsion," *Acta Mater.*, vol. 69, pp. 68–77, May 2014, doi: 10.1016/j.actamat.2014.01.036.

[45] L.-Y. Tian, R. Lizárraga, H. Larsson, E. Holmström, and L. Vitos, "A first principles study of the stacking fault energies for fcc Co-based binary alloys," *Acta Mater.*, vol. 136, pp. 215–223, Sep. 2017, doi: 10.1016/j.actamat.2017.07.010.

[46] B. Murty, M. Datta, and S. Pabi, "Structure and Thermal Stability of Nanocrystaline Materials," *Sadhana*, vol. 28, pp. 23–45, Feb. 2003, doi: 10.1007/BF02717124.

[47] J. Sort, J. Nogués, S. Suriñach, J. S. Muñoz, and M. D. Baró, "Correlation between stacking fault formation, allotropic phase transformations and magnetic properties of ball-milled cobalt," *Mater. Sci. Eng. A*, vol. 375–377, pp. 869–873, Jul. 2004, doi: 10.1016/j.msea.2003.10.186.

[48] D. A. Porter and K. E. Easterling, *Phase Transformations in Metals and Alloys, Third Edition (Revised Reprint)*. CRC Press, 1992.

[49] D. K. Belashchenko, V. V. Hoang, and P. K. Hung, "Computer simulation of local structure and magnetic properties of amorphous Co–B alloys," *J. Non-Cryst. Solids*, vol. 276, no. 1, pp. 169–180, Oct. 2000, doi: 10.1016/S0022-3093(00)00262-3.

[50] Y. Krimer, N. Aronhime, P. Ohodnicki, and M. E. McHenry, “Prediction of good glass forming ability in amorphous soft magnetic alloys by thermocalc simulation with experimental validation,” *J. Alloys Compd.*, vol. 814, p. 152294, Jan. 2020, doi: 10.1016/j.jallcom.2019.152294.

[51] M. E. McHenry and D. E. Laughlin, “19 - Magnetic Properties of Metals and Alloys,” in *Physical Metallurgy (Fifth Edition)*, D. E. Laughlin and K. Hono, Eds. Oxford: Elsevier, 2014, pp. 1881–2008.

CHAPTER 3: CRYSTALLIZATION CHARACTERISTICS IN CO-BASED MAGNETIC AMORPHOUS NANOCOMPOSITES

Alicia G. Koenig[a], Alex Leary[b], Ronald Noebe[b], Claudia Mewes[c], Tim Mewes[c], and Gregory B. Thompson[a]

[a] The University of Alabama, Department of Metallurgical & Materials Engineering, Box 870202 Tuscaloosa, AL 35473, USA

[b] NASA Glenn Research Center, Materials and Structures Division, Cleveland, Ohio 44135, USA

[c] The University of Alabama, Department of Physics & Astronomy, Tuscaloosa, AL 35473, USA

Abstract

The examination of the crystallization behavior of amorphous melt spun $Co_{(78-x)}Fe_2Mn_xB_{14}Si_2Nb_4$ (x = 0.5 and 6.0%) alloys has been undertaken as they are candidate materials for use in alternating current motors. Transmission electron microscopy (TEM) and atom probe tomography (APT) reveal the presence of precipitation of crystallites in the as-cast Mn 0.5% alloy which are not seen in the as-cast Mn 6.0% alloy. TEM and APT analysis of these alloys after annealing at 400°C for 10 minutes and 2 hours reveal the continuation of precipitation of Co-rich nanocrystallites from the matrix (≈ 3 – 5 nm), with little change in crystal structure, morphology, and chemical partitioning behavior as a function of either anneal time or alloy content. Short range ordering measurements of the pair distribution function by electron diffraction reveals a modification of the second nearest neighbor bonding in these crystallites that is explained by the metastable incorporation of Fe in these precipitates. TEM and x-ray diffraction analyses reveal that annealing at 400°C for 3 hours and 6 hours for Mn 0.5% and Mn

6.0%, respectively, resulted in a secondary precipitation of a $Mn_3(Co_{10}B_3)_2$ phase, which was hundreds of nanometers is size. These results imply that additional Mn solute suppresses crystallite nucleation and growth.

3.1 Introduction

The improvement of electric propulsion capabilities is of high priority in efforts to reduce air pollution generated by the combustion of fossil fuels [1]. However, this technology is currently limited by the weight of the required components [2] resulting in significant research to reduce the size and weight which increases the power density in electronic motors. One means to improve electronic motors is the optimization of the magnetic core alloys. This offers two major avenues to weight reduction. First, the reduction of power losses during the magnetic switching would increase the power density per unit mass [3]. And second, an increase in acceptable operating temperatures without core degradation would reduce the need for heavy cooling systems [4].

Typically, soft magnetic alloys are used in the core because of their notably low magnetic coercivity enabling an ease of magnetic switching. While conventional transformer cores for industrial power are ferrite and Si steels [4], such alloys suffer high losses when operating at high frequencies [5] and are unsuitable for electric motor cores. Rather, an alternative class of metal core alloys are metallic amorphous nanocomposites or MANCs. These are characterized by a fine dispersion of nanocrystallites embedded in a continuous amorphous matrix. While a decreasing crystallite size is nominally associated with an increase in coercivity, once the crystallite is $< \approx 100$ nm, the coercivity readily drops because of exchange coupling between the crystallites. These have been shown to have a higher power-to-loss ratio when operating at higher frequencies [5].

Several classes of MANC alloys are currently being investigated to fill this performance gap [6], [7]. These include the commercial names of FINEMET or VITROPERM and NANOPERM [8]. These MANCs are majority Fe-rich with additional elements being early

transition metals (such as Zr, Hf, and Nb) to impede crystallite growth by increasing the activation energies for diffusion and glass former elements like B and Si to stabilize the amorphous metal matrix phase. This complex composition then creates a variety of chemical partitioning behaviors between each species and their phase formation.

More recently, Co-based MANCs have emerged as promising candidates because of their high Curie temperature, allowing them to maintain their magnetic properties in a higher operating environment [9]. These alloys are melt spun into an amorphous matrix after annealed above primary crystallization peak but below the onset of secondary crystallization to promote the nanocrystalline precipitation. Leary et al. found a remarkable relationship between permeability and alloy composition in these alloys if various amounts of Mn is used coupled with the annealing being done while the MANC was under strain [10]. Atom probe analysis of these alloys by the authors have revealed that a change in crystallite density was present as a function of the Mn alloy composition [11], implying that a change in initial crystallite nucleation and growth behavior was probable. The increase in Mn content was at the expense of the Co content, this created a change in Co:B ratio resulting an in increased diffusivity that was proposed to influence the densification of the crystallites. However, the exact crystallite nucleation and growth mechanisms for these Co-based MANCs was not entirely understood. This work aims to clarify the early onset crystallization in these Co-based MANCs to elucidate how Mn content controls the early and extended stages of crystalline precipitation.

3.2 Materials and methods

Two alloys, $Co_{78-x}Fe_2Mn_xNb_4Si_2B_{14}$ (x = 0.5, 6.0 at.%) were melt-spun in air under a shielding atmosphere of Ar, generating amorphous ribbons with a thickness of 20 μm and width

of approximately 3 mm. For the balance of the paper, these two alloys will be referred to as Mn 0.5% and Mn 6.0%. This process was achieved using a large-scale, 5 kg planar flow caster. The interested reader is directed to reference [12] for additional processing details. These ribbons were sectioned and annealed in a vacuum tube furnace at a temperature of 400°C for 10 minutes, 1 hour, 2 hours, 3 hours, and 6 hours, with the details for the temperature selection discussed in the forthcoming results section.

Differential scanning calorimetry (DSC) was used to examine the thermal responses as the as-cast alloys underwent phase transitions to verify the precise temperature of the crystallization peaks. Here, small pieces of ribbon were placed in an alumina crucible which had previously been baked out at a temperature of 1000°C. The DSC was performed in a Setaram Labsys Evo. The samples were subjected to anneals to upward of 700°C, at heating rates of 10 K/min, 20 K/min, 30 K/min, and 40 K/min.

The structural phase determination was completed by X-ray and electron diffraction. For X-ray diffraction (XRD), a Bruker D8 Discover Diffractometer with a Co source was used and for electron diffraction, a FEI Tecnai F-20 (S)TEM operated at 200 keV was used. The XRD samples were mounted to a poly(methyl methacrylate) specimen holder using carbon tape whereas the TEM foil preparation was more involved. Here, a focused ion beam (FIB) liftout technique was employed to create specimens [13] in a TESCAN LYRA FIB-FESEM. Since ion damage from milling can occur, particular care was done in applying a final polish at 5 keV and 30 pA to reduce any Ga damage [14].

Atom probe tomography (APT) provided near atomic lattice rectification compositional analysis. The required needle shaped tip was prepared using a similar FIB lift out technique [13], with annular milling patterns used to shape an approximately 70 nm radius end using a TESCAN

LYRA, with the final milling steps being again at 5 keV and 30 pA to reduce potential damage from Ga^+ implantation [15]. The sharpened tips were then field evaporated in the CAMECA Local Electrode Atom Probe (LEAP) 5000XS, with a detector efficiency near 80%. The operating parameters of the LEAP consisted of a specimen set point of 40 K, laser pulse energy of 30 pJ, and pulse repetition rate of 625 kHz, with a per pulse detection rate of 0.5%. The APT datasets were reconstructed using CAMECA's Integrated Visualization and Analysis Software (IVAS) 3.8.0.

3.3 Results

Figure 3.1 details DSC curves for the Mn 0.5% alloy **(a)** and Mn 6.0% alloy **(b)** for heating rates between 10-40 K/min. For the purposes of this study, there are two major temperature ranges at which phase transitions appear to occur - the primary crystallization peak, whose onset occurs between 420-430°C, and secondary crystallization, which occurs at temperatures above 600°C. Because the desired magnetic properties for the alloy are severely degraded upon the onset of the secondary crystallization [16], we focused our attention on the range at which primary crystallization occurs.

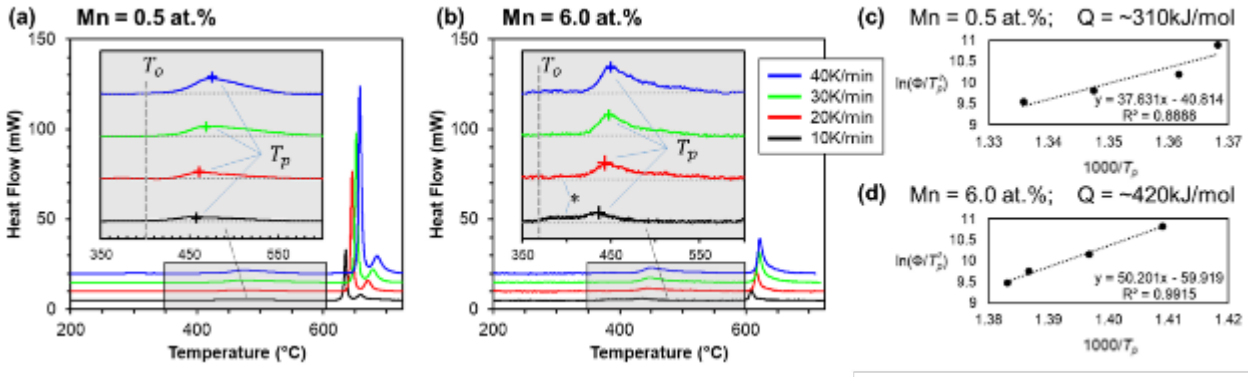

Figure 3.1 Calorimetry data for the Mn = 0.5% (a) and Mn = 6.0% (b) alloys. The inset graph is an expanded view of the indicated region. (c) and (d) show the Kissinger plots, a function of

heating rate Φ and marked central peak locations T_p , the slope of which can be used to estimate the activation energy Q of the phase transition. The asterisk in (b) marks the portion of the graph that indicates a secondary slope.

The primary inset in **Figure 3.1** provides a magnified view of the primary crystallization curve. The temperature corresponding with the approximate peak center is marked with a small tick mark, with this data being used to approximate the activation energy for the phase transition using the Kissinger method [17]. The equation is given by equation [1],

$$-\ln\left(\frac{\Phi}{T_p^2}\right) = -\ln\left(\frac{AR}{Q}\right) + \left(\frac{1}{T_p}\right)\left(\frac{Q}{R}\right) \qquad [1]$$

where measurement of Φ and T_p (the heating rate and temperature of the peak location, respectively) can be used to approximate the activation energy, Q; and A and R (R = 8.314 J·K^{-1}·mol^{-1}) are constants. From this, the activation energies for each peak were estimated to be $Q = \sim 310$kJ/mol and $Q = \sim 420$kJ/mol for the Mn 0.5% and Mn 6.0% alloys, respectively.

Based on the DSC, we selected an anneal temperature of 400°C as it was just prior to the onset of primary crystallization. Nucleation in these materials is a stochastic process that depends on an exponential activation barrier. Thus, in principle, a slightly lower temperature would enable experimental control in reducing the time to rapidly nucleate and grow the crystallite phase as the different species partition enabling specific characterization to be done at various extended time scales. Conversely, annealing at or higher temperatures than the primary crystallization temperature would cause rapid crystallization making it more difficult to capture these early onset behaviors.

XRD spectra for the as-cast and vacuum annealed ribbons are shown in **Figure 3.2**. The as-cast spectra for both the Mn 0.5% (**Figure 3.2(a)**) and Mn 6.0% (**Figure 3.2(b)**) are characterized by a single broad peak just above 2θ = 50°, with a significant contribution of an

amorphous signal evident by an even broader, modestly elevated intensity seen in each scan. Spectra for annealed samples ($t \leq 2$ hours) are very similar to those of the as-cast samples, with a slight increase in peak height relative to the spectrum background but little other indication of any changes.

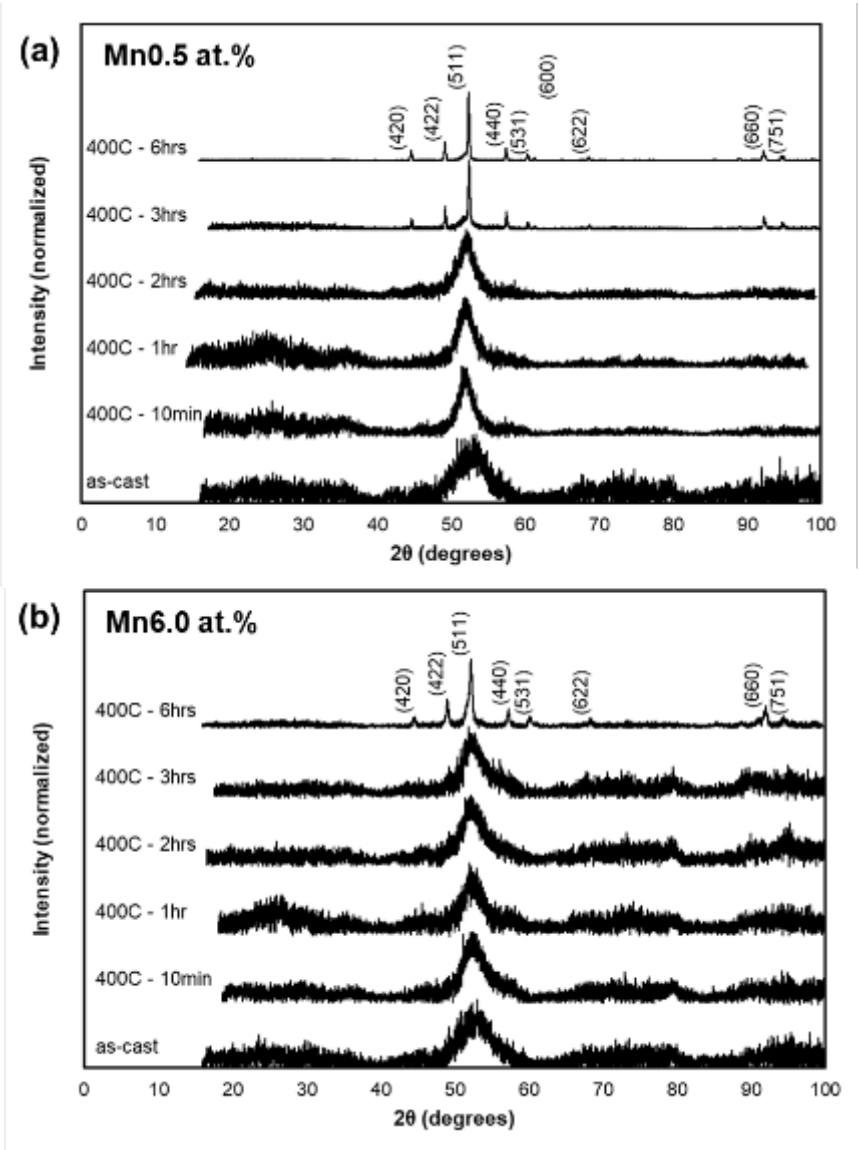

Figure 3.2 X-ray diffraction of as-cast and vacuum annealed Mn 0.5% (a) and Mn 6.0% (b) samples

In contrast, spectra for annealed samples ($t \geq 3$ hours and $t = 6$ hours for Mn 0.5% and Mn 6.0%, respectively) contain several sharp and distinct peaks, indicating the presence of strong crystalline diffraction. Indexing of these peaks match those of $Mn_3(Co_{10}B_3)_2$ [18]. This complex FCC boride phase has previously been shown to degrade the soft magnetic properties in magnetic alloys but only after annealing at the secondary crystallization peak [16], hence it was surprising to note it here after a much lower anneal temperature and modest annealing time.

Little change is seen in selected area electron diffraction [SAED] patterns gathered from the as-cast and vacuum annealed samples that have not yet shown evidence of the $Mn_3(Co_{10}B_3)_2$ precipitation. These patterns reveal a broad, diffuse inner ring with a few, more distinct outer rings, **Figure 3.3**. **Figure 3.3(a)-(h)** is a composite image, depicting one-eighth slices of from each of the various annealed conditions for the two compositions. In this construction, one can readily compare if potential shifts in the rings' diameter occur between each anneal state enabling a quick recognition of any lattice parameter shifts. In these conditions, no significant shifts were noted. Unlike the XRD data, the SAED patterns are more sensitive in resolving the other contribution of the crystallite phase, evident by the clear scattering intensity of the additional, distinct outer diameter rings. **Figure 3.3(i)** is taken from **Figure 3.3(c),** the Mn 0.5% / 2 hour sample. The diffraction rings index closely to an FCC structure and is consistent pattern for all conditions, even the as-cast state. Contrary to all other previous patterns, the Mn 0.5% / 3 hour annealed sample, **Figure 3.3(d)**, reveals distinct diffraction spots along with these prior rings. These spot reflections match diffraction planes from the identified boride phase above. The presence of spots (and not rings) confirms that the $Mn_3(Co_{10}B_3)_2$ phase would be significantly larger than FCC phase in the collected area of these diffracted regions. This would agree with the sharper XRD peak breadths seen in the XRD scan for this phase in this alloy and

annealing condition, **Figure 3.2(a)**. While this XRD scan for Mn 0.5 at% / 3 hour anneal clearly indicates the $Mn_3(Co_{10}B_3)_2$ phase, upon closer inspection of the XRD scan, a remnant amorphous scattered intensity (~ 20 to 30° 2θ) and broader base to the ~ 53° 2θ peak is present, indicating evidence of the retained amorphous phase, *i.e.*, the MANC is not fully crystallized. This too is an agreement with the TEM diffraction, **Figure 3.3(d)**, that retained the amorphous background signal is seen in all of the patterns, **Figure 3.3(a-h)**. Hence, at this condition, the alloy is not fully transformed into this boride phase.

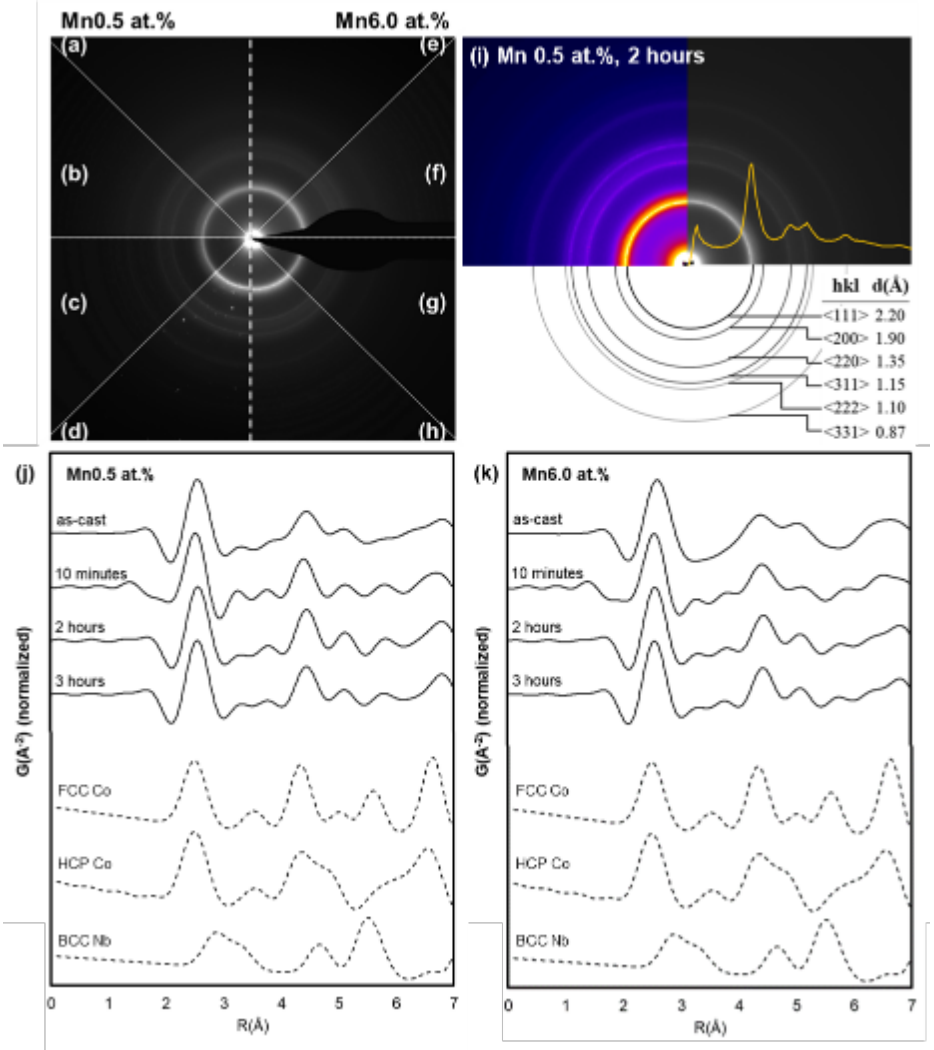

Figure 3.3 TEM SAED patterns of Mn 0.5% (a-d) and Mn 6.0% (e-h), divided into eighths and combined for both visual brevity and ease of comparison. The patterns for the as-cast, 10 minute anneal, 2 hour anneal, and 3 hour anneal samples can be seen in (a,e), (b,f), (c,g), and (d,h), respectively. (i) shows a broader view of one representative pattern (Mn 0.5%, 2 hour anneal) which has been further processed for visual clarity using LUTs. An overlayed graph shows the intensity of the average radial profile of the image, and below are markers for the location of identified rings which have been indexed and labeled. (j) and (k) show the atomic PDFs which have been derived from these diffraction patterns, as well as simulated PDFs for FCC Co, HCP Co, and BCC Nb prototype structures.

Recognizing the retention of the amorphous and small FCC crystallite phase through the annealing conditions, the atomic pair distribution function (PDF) has been calculated via selected area electron diffraction patterns using the ePDFSuite developed by NanoMEGAS [19]. This provides a measurement of the short-range ordering (SRO) present in the alloy. While FCC and HCP are close packed structures, the preference to designate the SRO towards FCC and not HCP is both the SAED pattern as well as the lack of a shoulder in the peak located at ≈ 4.9 Å , which would be present if it was HCP. Nevertheless, a notable deviation from either the FCC or HCP simulated structures is the appearance of a double peak around ≈ 3.5 Å, where there exists only a single peak in the simulated PDF for either FCC or HCP Co prototypes (see **Figure 3.3(j),(k)**). The only exception here is the as-cast Mn 6.0 at% alloy, **Figure 3.3(k)** where no peaks are located at this distance. This curve also has fewer oscillations, particularly in the 3-4 Å and 6-7 Å regions, indicating a lesser regularity in the periodicity of the pair distribution function implying a greater prevalence of disordered atomic arrangements. Upon annealing, the measured SRO is remarkably consistent within each alloy and between each alloy.

TEM bright field images of these alloys are presented in **Figure 3.4**. While both the Mn 0.5% and Mn 6.0% samples were intended to be an entirely glassy amorphous phases with a large degree of homogeneity, very small, randomly located crystallites (evident by diffraction contrast)

are found in the Mn 0.5% as-cast sample, **Figure 3.4(a)**. Such diffraction contrast was not seen in the Mn 6.0% sample which was devoid of any precipitation, **Figure 3.4(e)**.

There is a clear change in the microstructure after the 10-minute anneal, with both alloys exhibiting a homogeneous distribution of crystallites scattered throughout an amorphous matrix **Figure 3.4(b,f)**. These crystallites were the FCC indexed phase in the SAED patterns of **Figure 3.3**. There is little observable difference between the Mn 0.5% and Mn 6.0 at.% samples during these stages. Furthermore, annealing up to 2 hours for either alloy reveals consistent precipitate features with no notable changes (coarsening) since their initial presence, **Figure 3.4(c,g)**.

For the Mn 0.5% sample after 3 hours of annealing, very large crystallites ($d > 100$ nm) were sporadically located throughout the microstructure, **Figure 3.4(i)**, which are not found in the equivalently processed Mn 6.0% alloy **Figure 3.4(d,h)**. These crystallites are the $Mn_3(Co_{10}B_3)_2$ phase with the HRTEM image, **Figure 3.4(j)**, confirming the crystallinity by the presence of the lattice fringes. The larger crystallite size confirms the diffraction behavior of sharper peak breadths in the XRD scan, **Figure 3.3(a)**, and the spots in the SAED pattern, **Figure 3.4(h)**. While the larger boride crystallite has now precipitated in this matrix, the small FCC nano-crystallites are still retained as well, which agrees with the SAED pattern, **Figure 3.3(d)**.

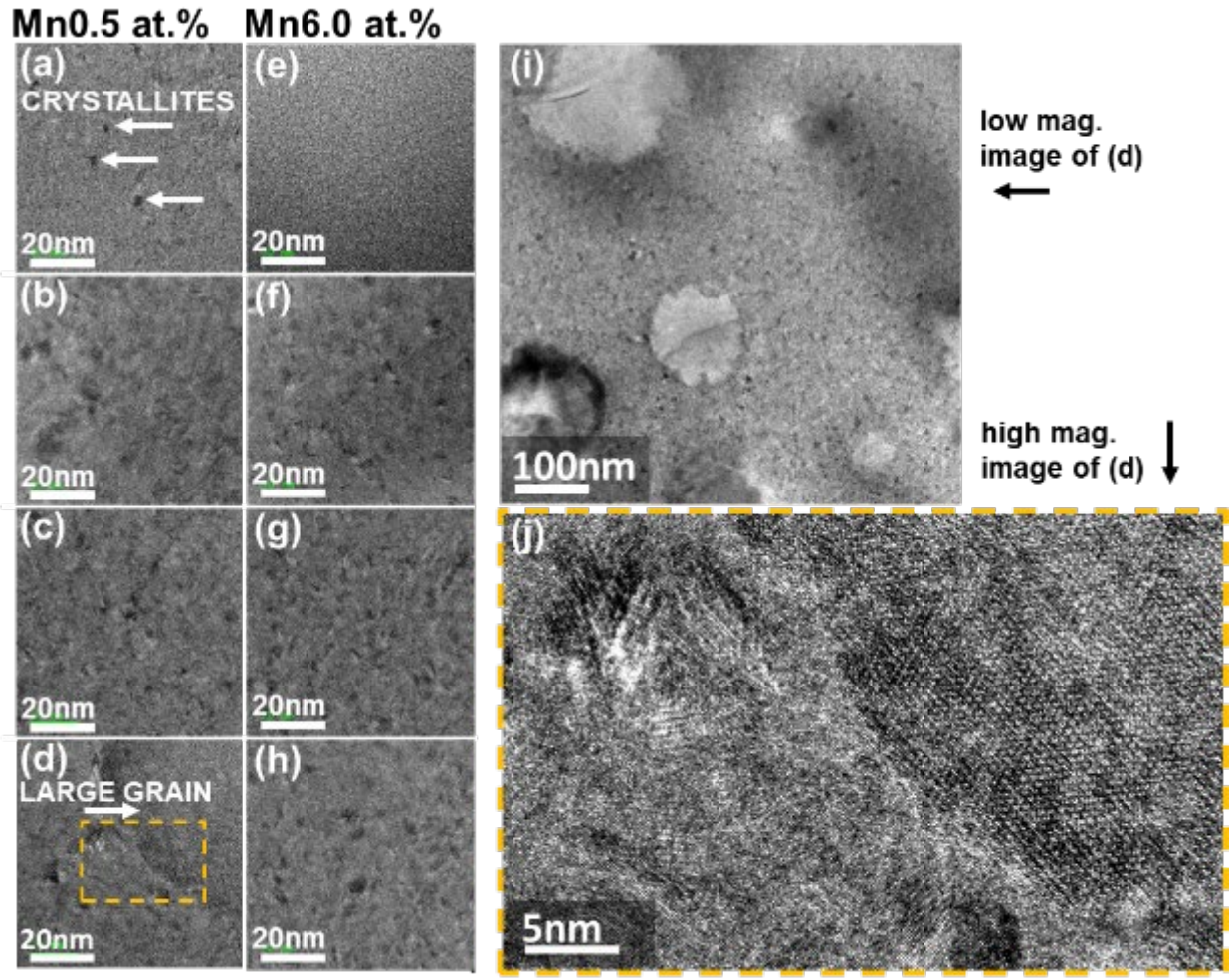

Figure 3.4 TEM bright field images of Mn 0.5% (a-d) and Mn 6.0% (e-h). The images of the as-cast, 10 minute anneal, 2 hour anneal, and 3 hour anneal samples can be seen in (a,e), (b,f), (c,g), and (d,h), respectively. A low magnification image of Mn 0.5%, 3 hour anneal is shown in (i), and a higher magnification image that same sample in (j).

Complementing the structural scattering and imaging of the phase, the composition analysis of the phases was completed by APT, **Figure 3.5**. The APT data revealed the presence of nanoscale inhomogeneities in the as-cast Mn 0.5% alloy evident by the changes the reconstructed density map, **Figure 3.5(a).** In the as-cast condition, one would anticipate a constant density reconstruction. This density variation is less pronounced in the as-cast Mn 6.0% alloy. Upon annealing, these high-density regions become more apparent in both alloys, but are

qualitatively more refined in size for the Mn 6.0% alloy, compare **Figure 3.5(a) ii** vs. **v** and **iii** vs. **vi**. **Figure 3.5(b)** and **(c)** shows the chemical frequency distribution analysis for as-cast states for each alloy respectively. For the Mn 0.5% alloy, the B and Co (observed) show significant deviation from the simulated binomial distributions, **Figure 3.5(b)**, indicating that these species are experiencing some degree of chemical partitioning. For the as-cast Mn 6.0%, **Figure 3.5(c)**, either no or very minimal deviation (for the B) from randomness is noted for each element, approximating a truly random solid solution. This clearly indicates a distinct chemical difference between the two alloys in this particular processed condition.

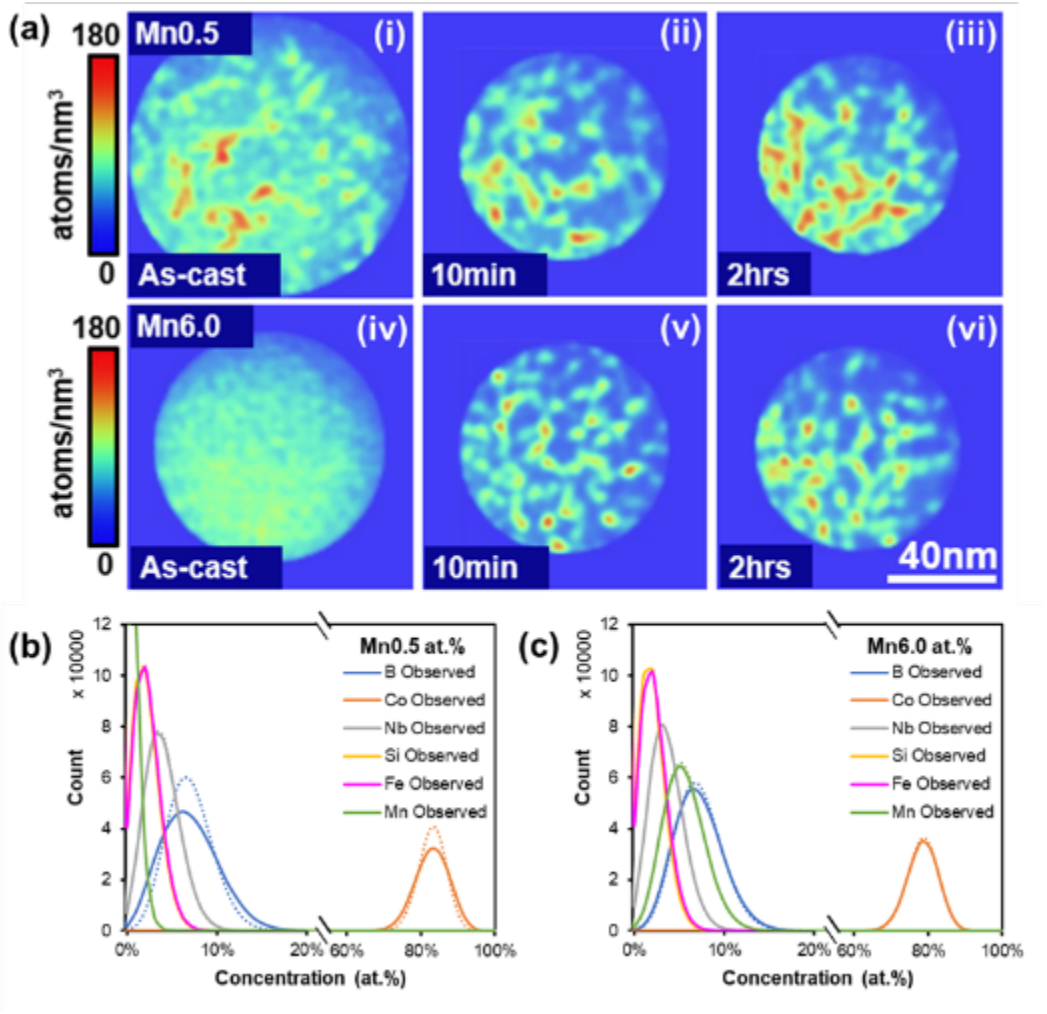

Figure 3.5 (a) 2D concentration maps, calculated from slices with thickness $z = 1$ nm. Concentration frequency distribution analyses of as-cast Mn 0.5% (b) and Mn 6.0% (c). Dashed lines represent the simulated binomial distributions for each element.

3.4 Discussion

3.4.1 Nucleation and growth of nanocrystalline grains

TEM and APT results have shown that the as-cast Mn 0.5% sample can be characterized as having a non-homogeneous microstructure (presence of nanoscale crystallite, **Figure 3.4(a)**) with a corresponding partitioned chemical distribution, at least for Co and B (**Figure 3.5(b)**). Prior reports have shown that Co favors the crystallite phase and B the amorphous phase [11].

With this partitioning, even the SRO behavior of the as-cast alloy revealed bond distances that trended the annealed sample, particularly the existence of the double peaks near 3.5 Å. These inhomogeneous regions must have formed during the spin-melting of the sample, prior to or during the rapid quenching of the ribbon against the cooled, spinning surface. This is quite surprising considering that the cooling rates are predicted to be ≈ 10^6 °C/s [20]. Upon annealing, additional crystallites formed and are of the same sizes throughout the microstructure, **Table 3.1**. These as-cast precipitates are likely not serving as heterogeneous sites for these future annealed crystallites; if so, one would expect a bimodal crystallite size distribution with the earlier formers growing with time. The as-cast Mn 6.0% alloy has a nearly perfect homogeneous solid solution mixture which was consistent in that no nanoscale crystallites were found in this microstructure. Furthermore, the SRO measurements of the Mn 6.0% alloy contained fewer fluctuations in the PDF than measurements of any of its annealed samples and had an absence of the double peaks near 3.5 Å, which only appeared upon this composition annealing.

After annealing for 10 minutes, both alloys demonstrated significant changes in microstructure with the presence of nanoscale precipitates. Inspection of the TEM bright field imaging, **Figure 3.4(b,f)**, shows regularly occurring regions marked by changes in diffraction contrast, implying the presence of crystallites. Furthermore, upon closer inspection of these regions, **Figure 3.4(j)**, one can see lattice fringes which further justify the definition of these regions as crystalline. The SAED patterns, **Figure 3.3(a)-(h)**, confirm agreement to the FCC Co structure as well. While bulk Co is thermodynamically stable as HCP, there are several papers that report FCC stabilization for small sizes, i.e., < 10 nm [21]–[23] which is well within the size regime of the measured Co-rich crystallites in the bright field images of **Figure 3.4** and APT measurements tabulated in **Table 3.1**. It is highly probably considering size effects to

thermodynamic equilibrium that the FCC Co here is the thermodynamically stable structure. The crystal stability change for such smaller sizes compared to the bulk is contributed to the influence of a higher fraction of atoms being on the surface in the sub-10 nanometer regime, where surface energies are comparable to volumetric energy considerations [24]. Notably even the PDF behavior changes after the 10-minute anneal for the Mn 6.0% alloy, with the SRO fluctuations for this and the other annealed states as well as the lower Mn alloy matching reasonably well to the FCC prototype structure over extended SRO periodicities, **Figure 3.3**. The increased scattering periodicity supports stabilization of this structure over longer ranges.

Comparing the crystallite sizes between the two compositions, **Table 3.1**, their sizes are within each other's standard deviation, thus any growth (once formed) is statistically similar. However, the Mn 0.5% volume fraction has a slightly higher value than that of the Mn 6.0% and this trend continues and becomes even larger with annealing time. While these volume fraction measurements do not have an error as they are made with a single APT data set for each alloy state, the trend would be consistent with what is observed in the as-cast condition. Since the Mn 0.5% has already formed some fraction of nanocrystallites in the as-cast microstructure, and these crystallites are not acting as heterogeneous nucleation sites for subsequent precipitation, this alloy, in effect, has a 'head start' in precipitation slightly increasing its volume fraction with time as compared to the Mn 6.0% alloy. Furthermore, this volume fraction difference actually increases with the longer annealing time, **Table 3.1**, suggesting that nucleating the crystallite phase in Mn 0.5% alloy is easier than in the Mn 6.0% alloy. This is again supported that the lower Mn alloy precipitates the other crystalline phase $Mn_3(Co_{10}B_3)_2$ at an earlier time than the higher Mn alloy.

Revisiting the DSC results in this context, the estimated activation energy for primary crystallization was 310 kJ/mol for the Mn 0.5% and was 420 kJ/mol for the Mn 6.0%. This would imply that it requires less energy for the primary phase transformation to occur in a lower Mn content alloy. Additionally, closer examination of **Figure 3.1(b)** reveals what may be a subtle phase transition prior to primary crystallization. This is only observed in the slowest heating rate in the slowest precipitating alloy (Mn 6.0%), but there exists a small region preceding primary crystallization which appears to have a separate and unique slope (marked by the asterisk in the figure). This onset could be the initial clustering that leads to precipitation. Its absence in either the Mn 0.5% alloy and/or higher heating rates for either alloy suggests that to observe this effect, one requires 'sluggish kinetics' and sufficiently slow heating that is offered by the Mn 6.0% alloy. This phase transition becomes more difficult to capture at faster heating rates since the change in temperature occurs more quickly, potentially obscuring the signal in the larger primary crystallization peak.

It was also noted that the crystallization onset temperature (T_o, corresponding to the onset of the peak) does not change regardless of the heating rate. While there may be some nucleation/growth mechanism explanation for this behavior, it should be noted that T_o has generally been found to be less sensitive to changes in heating rate than T_c, the crystallization temperature [25]. For this reason, the authors are reluctant to attribute any particular interpretation of the lack of relationship between the onset temperature, T_o, and the heating rate.

Both alloys, after being subjected to 1-hour and 2-hour anneals revealed little visible change in microstructure, *i.e.*, only nanocrystallites are present in the amorphous matrix. This is confirmed through the TEM bright field images (**Figure 3.4(c,g)**), XRD spectra (**Figure 3.2**), and PDF ordering measurements (**Figure 3.3(j,k)**) for both alloys. However, using atom probe

isodensity surfaces, the approximate size and volume fraction of the crystallites was able to be distinctly estimated, whereupon the volume fraction changes within and between the alloys was quantified, **Table 3.1**. Using the isodensity surfaces for these measurements, the proximity histogram revealed the chemical partitioning between the crystalline and amorphous phases, **Figure 3.6**. In all cases, the Co and Fe enriched the crystallite phase and the compositional profiles between the annealed times are relatively equivalent to each other. The only notable significant composition profile variation is seen in the Mn 0.5% as-cast to annealed state, where the Co and B compositional profiles become more pronounced with annealing. Note, the as-cast Mn 6.0% is not presented since it did not form any measurable compositional variation to compare to the annealed conditions, where a compositional partition behavior was evident. Together, these observations indicate that once a crystallite is formed, it very quickly ceases to evolve in both size and chemical composition.

Table 3.1 Comparing densities, crystallite size, and crystalline volume fraction using APT

Sample ID	**Heat Treatment**	ρ *(atoms/nm3)*		$(\rho_C-\rho_B)/\rho_B$	Crystallite diameter (nm)		Vol. Frac. (%cryst.)
		Bulk	Crystallite				
Mn = 0.5	as-cast	92 ± 24	195	2.1	3.8	13	
	10 minutes, 400C	72 ± 17	168	2.3	3.4	27	
	2 hours, 400C	84 ± 14	189	2.3	3.2	35	
Mn = 6.0	as-cast	81 ± 6	-	-	-	-	
	10 minutes, 400C	65 ± 23	164	2.5	3.8	25	
	2 hours, 400C	81 ± 19	180	2.2	4	30	

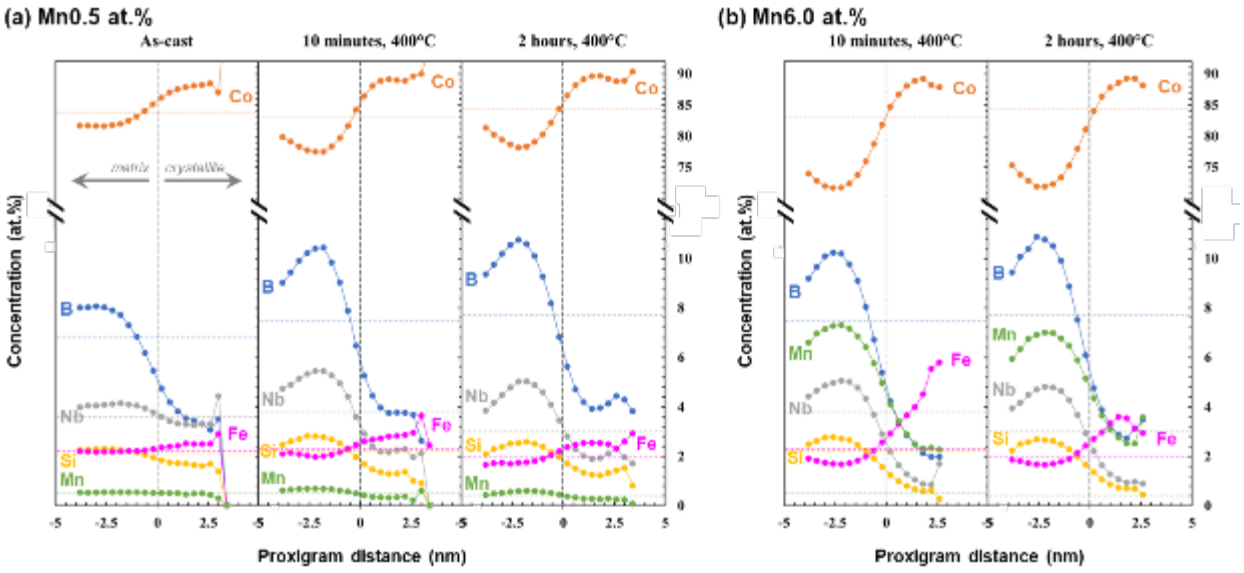

Figure 3.6 Proxigrams calculated via isodensity surface. Isodensity values for each graph from left to right were 100.549, 98.000, 96.900, 100.728, and 101.540 atoms/nm^3.

The incorporation of Fe into the Co-rich may also explain the FCC solid solubility that these two species share at elevated temperature. Reviewing the bulk equilibrium phase diagram for Co-Fe, **Figure 3.7**, they share a high temperature FCC solid solubility at temperatures > ≈ 422°C. While our anneal was slightly lower at 400°C, this solid solubility field is based on bulk equilibrium thermodynamics and would be modestly lowered in an analogous manner to the depression of the melting temperature in nanoscale particles [26] and the stabilization of FCC Co discussed previously. Thus, it is not inconceivable that this would explain Fe's incorporation into the Co crystallite at 400°C, **Figure 3.6**, as well as its incorporation previously reported for much higher anneals at 520°C [11], with this latter temperature well within the bulk equilibrium stability region.

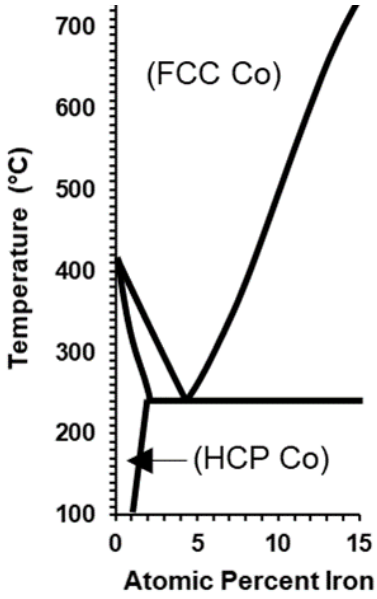

Figure 3.7 Sub-section of the Co-Fe phase diagram adapted from reference [27]

While these nanoscale structures may change conventional thermodynamic phase boundaries for the FCC solid solubility, it is not clear, upon cooling if the nominally ferric (BCC) Fe would still prefer to remain in solid solution with FCC Co. At least for the bulk HCP Co phase, where HCP and FCC are equivalent close packed structures, Fe's solubility at room temperature in HCP Co is $< \approx 0.5\%$, **Figure 3.7**. In our Co-rich crystallites, the proximity histogram profiles, **Figure 3.6**, show Fe concentrations of ≈ 3 at.%. This would indicate that Fe would prefer to partition out of similar stabilized close packed FCC structure but was unable to do so considering kinetic considerations as the sample cooled rapidly after being annealed. This is equivalent in how similar Fe entrapment is reported in Co-rich clusters that have been annealed and cooled from 520°C [11].

The retention of Fe in the FCC Co lattice places the Co-rich crystallite now in a non-equilibrium state creating bonding distortions that are manifested through different bonding

lengths, such as double peaks in the SRO. A prototype Nb BCC SRO pattern has also been included in **Figure 3.3(j)** and **(h)** to the Co close packed FCC and HCP prototypes. Comparisons of these prototypes in the secondary nearest neighbor bond location reveals a clear and distinct peak difference between BCC and the close packed structures that resembles the double peak albeit slightly skewed in position from ideal. Hence, the super saturation presence of Fe in Co may be creating this localized SRO distortion, with any longer-range SRO fluctuations created by BCC damped out because it is not a preferred structure for Co. Higher order SRO fluctuations are indictive of longer-range periodicity of a particular structure. The lack of any BCC evidence in the SAED patterns would further support this claim of only very local SRO behavior and highlights the sensitivity and insight ePDF measurements can provide in these types of nanoscale diffraction. While these arguments are arguably speculative, the SRO measurement in this secondary nearest neighbor region coupled with the APT compositional data and known bulk phase stability behavior for Co-Fe offers a possible explanation for the double peaks and a potential fruitful area for future computational investigations.

Since the crystallites experience no measurable change in size with time, but the volume fraction is increasing, **Table 3.1**, then the crystallite number density must be increasing. This would support the argument that the alloys must be experiencing a constant nucleation rate when annealed at this temperature. For this to hold true, crystallite growth must be suppressed not by a site saturation mechanism(s) but by the alloy chemistry itself, *i.e.*, the stabilization of the amorphous matrix by the glass-forming elements and the suppression of growth by the presence of the transition metal Nb [8].

While we have discussed the crystallite formation as nucleation and growth, a martensitic mechanism has also been proposed to form these nanoscale precipitates because of the lack of

long-range diffusion. The small volume of the precipitates and relative invariance of the compositional evolution of the precipitate chemistry after formation characterized here are potential characteristics for such a transformation. However, a true martensitic transformation is described as a 'military transformation' since a synchronized shearing is required for the atoms in an existing crystalline lattice, which is nonexistent in an ideal as-cast amorphous MANC matrix. More likely if this is the transformation mechanism, it would be similar to a massive transformation, sometimes referred to as a 'diffusionless civilian transformation' [28]. Here the atoms experience randomly orientated or independent local displacements (*i.e.*, civilian motion) during redistribution that form the new phase, with the new phase not having an orientation relationship with the matrix phase. In the case of MANCs, the intergranular amorphous region would ensure the non-orientation relationship criterion. For a massive transformation event, a sufficient undercooling condition is needed, which is also meet by the solutes being in a vitrified as-cast condition. Nevertheless, these proposed 'diffusionless' mechanisms have only been reported in Co-rich MANCs that were subjected to a strain while being annealed, which is not the case for the current alloys studied. While similarities in the 'final microstructure and composition' of the nanocrystallites exist between nucleation and growth and diffusionless transformation pathways, the compositional profile evolution observed between the as-cast and the 10 min. anneal for the Mn 0.5% alloy directs us towards the transformation being more of a diffusional based mechanism.

3.4.2 Nucleation and growth of $Mn_3(Co_{10}B_3)_2$

Upon annealing for 3 hours for the Mn 0.5% and 6 hours for the Mn 6.0%, a new crystallite phase formed, *i.e.*, $Mn_3(Co_{10}B_3)_2$. While the nanocrystallites above are also present

along with this phase, **Figure 3.4(d,j)**, this new phase rapidly coarsened and is significantly larger than the early onset precipitates. The retention of these nanocrystallites suggest that they are not the incubators for the precipitation this boride phase.

The formation of this boride is not unprecedented in MANCs. Previously, they are noted to occur to nucleate and grow during secondary crystallization at higher temperatures (T > 600°C) [29]. The formation and growth of this phase does suggest that it is an equilibrium structure this alloy is driven towards. Being a boride-based phase, which promotes the glassy phase formation, may explain why it forms at higher temperature or, as in this study, simply needs longer times at lower temperatures. Furthermore, this suggest that this phase has a higher activity energy to overcome, with its delayed precipitation in the Mn 6.0% as compared to Mn 0.5% contributed to the more sluggish kinetics already noted in this alloy with higher Mn content.

Once this phase forms, it rapidly grows. To explain the rapid coarsening as compared to the Co-rich nanocrystallites, it is believed to be a result of its highly exothermic phase transformation. Reviewing the DSC scans in **Figure 3.1**, the secondary crystallization peak, where this phase is known to occur, has a much higher exothermic energy release peak than the primary crystallization peak at lower temperatures. With this heat release, it promotes rapid coarsening with the ultimate limit in controlling its size imposed by the long-rage diffusivity necessary to grow the precipitate once it formed and the exothermic heat has been expended.

The unexpected formation of this phase with extended annealing at modest temperatures of 400°C does suggest caution for these Co-rich MANCs being used in warm temperatures for extended times. This is because this boride phase is typically undesirable for high frequency applications [16]. What is particularly interesting is that Co-rich MANCs of equivalent

compositions that have been annealed at 520°C and quenched but then exposed to similar annealing temperatures and times as this study have not reported this boride phase formation [16]. This may suggest peculiar differences in continuous low temperature processing verses more conventional high temperature, short anneal times on the microstructural stability.

3.5 Conclusion

In this paper, the crystallization of the MANC $Co_{78-x}Fe_2Mn_xNb_4Si_2B_{14}$ with both 0.5 and 6.0% Mn content has been reported via a combination of TEM, APT, and DSC. It has been shown that the lower Mn alloy is non-homogeneous in the as-cast state. Upon annealing a higher density of Co-rich crystallites form. Similarly, for the higher Mn content alloy, these nanocrystallites form but only after annealing. In all cases, crystallite size remains relatively invariant near 3 to 5 nm but with increasing volume fraction, sugging a constant nucleation condition. The nanocrystallites were identified as FCC structures, which is a reported stabilized structure for nanoscale Co particles. The size effect on Co also is believed to result in a depression of the solid solubility with Fe incorporating it within its lattice. However, upon cooling, the Fe is retained in the crystallite resulting in a distortion of the second nearest neighbor bond distances as measured in the pair distribution function by electron diffraction. Upon extended heating of 3 hours and 6 hours for the Mn 0.5% and Mn 6.0% alloys, respectively, the $Mn_3(Co_{10}B_3)_2$ formed and was on the order of hundreds of nanometers in size. The suppression of the nanoscale Co-rich precipitate and sluggish formation of the coarser boride phase revealed microstructural indications that Mn retards the nucleation and growth behavior of both primary and secondary crystallization phases.

Acknowledgements

This work was supported by NASA CAN 80NSSC18M0023. Further, we would like to acknowledge the University of Alabama Analytical Research Center and staff. Additional support for this work came from the NASA Advanced Air Transport Technology Project, Electrified Aircraft Powertrain Technologies Subproject.

References

[1] L. Gipson, "NASA Tests Machine to Power the Future of Aviation Propulsion," *NASA*, Aug. 09, 2021. http://www.nasa.gov/aeroresearch/nasa-tests-machine-to-power-the-future-of-aviation-propulsion (accessed Apr. 11, 2022).

[2] "Electrified Aircraft Propulsion (EAP)," *Glenn Research Center | NASA*. https://www1.grc.nasa.gov/aeronautics/eap/ (accessed Apr. 18, 2022).

[3] R. Jansen, C. Bowman, A. Jankovsky, R. Dyson, and J. Felder, "Overview of NASA Electrified Aircraft Propulsion (EAP) Research for Large Subsonic Transports," in *53rd AIAA/SAE/ASEE Joint Propulsion Conference*, American Institute of Aeronautics and Astronautics, 2017. doi: 10.2514/6.2017-4701.

[4] J. M. Silveyra, E. Ferrara, D. L. Huber, and T. C. Monson, "Soft magnetic materials for a sustainable and electrified world," *Science*, vol. 362, no. 6413, Oct. 2018, doi: 10.1126/science.aao0195.

[5] A. Leary, P. R. Ohodnicki, and M. McHenry, "Soft Magnetic Materials in High-Frequency, High-Power Conversion Applications," *JOM J. Miner. ...*, vol. 64, Jul. 2012, doi: 10.1007/s11837-012-0350-0.

[6] P. C. Sarker, M. R. Islam, Y. Guo, J. Zhu, and H. Y. Lu, "State-of-the-Art Technologies for Development of High Frequency Transformers with Advanced Magnetic Materials," *IEEE Trans. Appl. Supercond.*, vol. 29, no. 2, pp. 1–11, Mar. 2019, doi: 10.1109/TASC.2018.2882411.

[7] A. Srivastava, K. Cole, A. Wadsworth, T. Burton, C. Mewes, T. Mewes, G. B. Thompson, R. Noebe, and A. M. Leary, "Broadband characterization of stress induced anisotropy in nanocomposite Co74.6Fe2.7Mn2.7Nb4Si2B14," *J. Magn. Magn. Mater.*, vol. 500, p. 166307, Apr. 2020, doi: 10.1016/j.jmmm.2019.166307.

[8] M. McHenry, F. Johnson, H. Okumura, T. Ohkubo, V. Ramanan, and D. Laughlin, "The kinetics of nanocrystallization and microstructural observations in FINEMET, NANOPERM and HITPERM nanocomposite magnetic materials," *Scr. Mater. - Scr. MATER*, vol. 48, Apr. 2003, doi: 10.1016/S1359-6462(02)00597-3.

[9] P. R. Ohodnicki, J. Long, D. Laughlin, M. McHenry, V. Keylin, and J. Huth, "Composition dependence of field induced anisotropy in ferromagnetic (Co,Fe)89Zr7B4 and (Co,Fe)88Zr7B4Cu1 amorphous and nanocrystalline ribbons," *J. Appl. Phys.*, vol. 104, pp. 113909–113909, Jan. 2009, doi: 10.1063/1.3021141.

[10] A. Leary, V. Keylin, A. Devaraj, V. DeGeorge, P. Ohodnicki, and M. E. McHenry, “Stress induced anisotropy in Co-rich magnetic nanocomposites for inductive applications,” *J. Mater. Res.*, vol. 31, no. 20, pp. 3089–3107, Oct. 2016, doi: 10.1557/jmr.2016.324.

[11] A. G. Koenig, D. Tweddle, A.M. Leary, R. Noebe, C. Mewes, T. Mewes, and G.B. Thompson, “Evaluating the effect of Mn composition on chemical partitioning in Co(78−x)Fe2MnxB14Si2Nb4 magnetic amorphous nanocomposites,” *J. Alloys Compd.*, vol. 875, p. 159976, Sep. 2021, doi: 10.1016/j.jallcom.2021.159976.

[12] A. Leary, “Mechanical Processing of Soft Magnetic Nanocomposites,” Ph.D. Materials Science and Engineering, Carnegie Mellon University, Pittsburgh, PA, 2016.

[13] K. Thompson, D. Lawrence, D. J. Larson, J. D. Olson, T. F. Kelly, and B. Gorman, “In situ site-specific specimen preparation for atom probe tomography,” *Ultramicroscopy*, vol. 107, no. 2–3, pp. 131–139, Mar. 2007, doi: 10.1016/j.ultramic.2006.06.008.

[14] K. Thompson, B. Gorman, D. Larson, B. Leer, and L. Hong, “Minimization of Ga Induced FIB Damage Using Low Energy Clean-up,” *Microsc. Microanal.*, vol. 12, pp. 1736–1737, Aug. 2006, doi: 10.1017/S1431927606065457.

[15] P. J. Felfer, T. Alam, S. P. Ringer, and J. M. Cairney, “A reproducible method for damage-free site-specific preparation of atom probe tips from interfaces,” *Microsc. Res. Tech.*, vol. 75, no. 4, pp. 484–491, Apr. 2012, doi: 10.1002/jemt.21081.

[16] G. Herzer, “Soft magnetic nanocrystalline materials,” *Scr. Metall. Mater.*, vol. 33, no. 10, pp. 1741–1756, Dec. 1995, doi: 10.1016/0956-716X(95)00397-E.

[17] H. E. Kissinger, “Variation of peak temperature with heating rate in differential thermal analysis,” *J. Res. Natl. Bur. Stand.*, vol. 57, no. 4, p. 217, Oct. 1956, doi: 10.6028/jres.057.026.

[18] A. Jain *et al.*, “Commentary: The Materials Project: A materials genome approach to accelerating materials innovation,” *APL Mater.*, vol. 1, no. 1, p. 011002, Jul. 2013, doi: 10.1063/1.4812323.

[19] “ePDF Applications,” *Nanomegas*. https://nanomegas.com/literature/epdf-applications/ (accessed Apr. 22, 2022).

[20] V. I. Tkatch, A. I. Limanovskii, S. N. Denisenko, and S. G. Rassolov, “The effect of the melt-spinning processing parameters on the rate of cooling,” *Mater. Sci. Eng. A*, vol. 323, no. 1, pp. 91–96, Jan. 2002, doi: 10.1016/S0921-5093(01)01346-6.

[21] E. A. Owen and D. M. Jones, “Effect of Grain Size on the Crystal Structure of Cobalt,” *Proc. Phys. Soc. Sect. B*, vol. 67, no. 6, pp. 456–466, Jun. 1954, doi: 10.1088/0370-1301/67/6/302.

[22] M. Hillenkamp, S. Oyarzún, N. Troc, J. Ramade, F. Tournus, V. Dupuis, and V. Rodrigues, "Size effects of the magnetic anisotropy of fcc cobalt nanoparticles embedded in copper," *Eur. Phys. J. D*, vol. 71, no. 12, p. 330, Dec. 2017, doi: 10.1140/epjd/e2017-80299-x.

[23] P. van Helden, I. M. Ciobîcă, and R. L. J. Coetzer, "The size-dependent site composition of FCC cobalt nanocrystals," *Catal. Today*, vol. 261, pp. 48–59, Mar. 2016, doi: 10.1016/j.cattod.2015.07.052.

[24] G. B. Thompson, R. Banerjee, and H. L. Fraser, "Tuning phase stability in nanocomposite multilayers," *Appl. Phys. Lett.*, vol. 83, no. 17, pp. 3471–3473, Oct. 2003, doi: 10.1063/1.1620671.

[25] "Onset Temperature — Website." https://thermalmaterials.org/wiki-pcm/onset-temperature (accessed Jun. 05, 2022).

[26] F. Gao and Z. Gu, "Melting Temperature of Metallic Nanoparticles," in *Handbook of Nanoparticles*, M. Aliofkhazraei, Ed. Cham: Springer International Publishing, 2016, pp. 661–690. doi: 10.1007/978-3-319-15338-4_6.

[27] H. Okamoto, "Co-Fe (Cobalt-Iron)," *J. Phase Equilibria Diffus.*, vol. 29, no. 4, pp. 383–384, Aug. 2008, doi: 10.1007/s11669-008-9345-5.

[28] H. I. Aaronson, "Mechanisms of the massive transformation," *Metall. Mater. Trans. A*, vol. 33, no. 8, pp. 2285–2297, Aug. 2002, doi: 10.1007/s11661-002-0352-6.

[29] G. Herzer, "Nanocrystalline Soft Magnetic Alloys," in *Handbook of Magnetic Materials*, 1st ed., vol. 10, K. H. J. Buschow, Ed. Elsevier Science B.V., 1997, pp. 415–462. Accessed: Mar. 31, 2020. [Online]. Available: https://www.elsevier.com/books/handbook-of-magnetic-materials/buschow/978-0-444-82599-5

CHAPTER 4: EVALUATING SPECKLE PATTERNS FOR DIGITAL IMAGE CORRELATION IN TRANSMISSION ELECTRON MICROSCOPY

Alicia G. Koenig[a], Thomas Koenig[a], Garritt Tucker[b], and Gregory B. Thompson[a]

[a] The University of Alabama, Department of Metallurgical & Materials Engineering, Box 870202 Tuscaloosa, AL 35473, USA

[b] Colorado School of Mines, Department of Mechanical Engineering, Golden, CO 80401

Abstract

This work examines the capabilities of digital image correlation of amorphous thin films characterized *in situ* under tension in a transmission electron microscopy environment. During sample preparation, an amorphous C film is exposed to a Ga^+ ion beam, introducing Ga contamination to the film. The introduction of thermal shock allows the Ga contamination to precipitate as a fine dispersion of visible clusters, which aid in the ability of digital image correlation algorithms to map displacement and deformation immediately preceding fracture.

4.1 Introduction to traditional digital image correlation

Digital image correlation (DIC) is an analytical technique for mapping surface deformation using landmark registration and tracking algorithms [1]. This technique can be applied to an optical image series of a specimen undergoing mechanical testing to map the

displacement of discrete points within a specified region of interest (ROI). This data can then be used to generate maps of deformations, strains, velocities, etc., relative to some user-defined baseline state as a function of time.

In traditional DIC, a speckling pattern is applied to the sample surface. The sample is then subjected to mechanical testing while the patterned surface(s) are recorded using optical cameras. In post-processing of these videos, automated algorithms are used to simultaneously track multiple unique markers within the speckling pattern using specialized software packages. These markers guide and optimize the tracking of discrete regions, or a grid of individual facets each containing a unique speckle pattern, along the plane of the deformed surface [2]. This tracking algorithm is more effective when the speckling patterns have high contrast relative to the sample surface, relatively uniform size, ~50% surface coverage, and a degree of shape anisotropy [3].

There exist many methods for creating these speckling patterns, each of which is dependent on material, scale, reflectivity, and other factors [3]. Some general examples include stenciling, stamping, and spray painting, but numerous other creative techniques can be applied in niche situations where drying time, pattern peeling, etc. are inhibiting factors [4]. In smaller-scale experiments, work has been done using electron beam lithography and focused ion beam (FIB) milling and deposition [5]. One important limitation is that the applied speckle pattern must not alter the deformation behavior of the specimen and must be assumed to deform conformably with the specimen surface. After all, the speckle pattern is merely a tool for enhancing computer vision. Additionally, an ideal speckle would occupy a minimum of 3 pixels and is spaced such that there are a minimum of 3 speckles in each subset or facet of the analysis

grid [6]. Larger speckles may not necessarily negatively affect accuracy and precision in identification and tracking but may slow overall computation time.

4.1.1 DIC in electron microscopy

DIC was originally developed for the analysis of optical data gathered with carefully controlled lighting environments, speckle patterning methods, and camera configurations. Traditional application of this technique becomes problematic when applied to electron microscopy, where imaging methods and signal processing become more complex [7]. Image collection techniques such as scanning electron microscopy (SEM) and scanning transmission electron microscopy (STEM) utilize a rastered data collection method that scans an ROI line-by-line for each image. This adds a time delay between data collected at the top and bottom of an image, which can distort or even remove data from consideration in an *in-situ* experiment utilizing DIC, depending on the relative speeds of image collection and deformation behaviors [8]. Additionally, diffraction-based mechanisms responsible for creating contrast such as phase, defects, and grain orientation are also sensitive to strain and deformation, resulting in changes in contrast [9]. Because the algorithm is searching for and tracking regions of high contrast relative to background, intrinsic changes in contrast of the sample can be confusing and misleading, resulting in data loss and erroneous displacement measurements.

Two recent works have been found which attempt to apply DIC techniques to transmission electron microscopy (TEM) images. To mitigate the effects of the variable diffraction contrast, which is largely attributed to rotation and deformation of crystalline phases, both works have focused on amorphous silicon-based films. Amorphous films contain an inherent speckling pattern that is based on diffraction contrast from regions of higher short-range

ordering [10], [11]. Wang et. al. [12] examined the application of DSC analysis to pure and lithiated amorphous Si. The authors evaluated the using only the native amorphous speckle pattern. Strain was applied to a tensile specimen using an *in-situ* push-to-pull device. The results indicated that the error of the DIC measurements were on the order of 0.1% and thus validated the technique. A more recent study examined deformation in amorphous silica via picoindentation using both DIC and particle tracking (PT). Zhang et. al. [9] applied a speckle pattern via the deposition and heat treatment of Au nanoparticles, creating speckles of around 40nm in diameter. Deformation of the specimen was induced using a picoindenter; results indicated that both PT and DIC using the Au nanoparticles generated comparable displacement measurements.

4.2 Objective and design of the study

The goal of this study is to develop a more refined speckle pattern for higher resolution in displacement mapping. A secondary objective is to compare the efficacy of an applied speckle pattern with that of the native speckle present in amorphous films. Additionally, the specimens examined here have been pulled to fracture, allowing the examination of extreme stress response behavior leading up to the fracture event. Finally, we have compared our local and global strain values with those of amorphous C in literature.

4.2.1 Incorporating MEMS devices for thermomechanical loading

The microelectromechanical system (MEMS) used was a comb-driven device supported by Z-shaped Si springs which support the dual stages and provide resistive heating when a current is applied. A tensile load can be applied to a mounted specimen by supplying a voltage to

the comb structures, which will be repelled from one another, driving the stages to separate. Comprehensive description of similar devices are provided in [13],[14]. The devices were then epoxied into a custom carrier fit to a Hummingbird 8-pin Electrical Biasing Holder and wire-bonded to the gold pads with 1 mil Au wire. A thermal shock was applied to facilitate precipitation of Ga speckles; the specimens were subsequently loaded at a stress rate of ≈ 10 $MPa \cdot s^{-1}$.

4.2.2 Materials and methods

Amorphous C was selected for their ease of access and average film thickness, which at ~25 nm is ideal for imaging. The thin film specimens were prepared for TEM through a focus ion beam (FIB) milling lift-out technique using a TESCAN LYRA FIB-FESEM. The samples were extracted from the plane-normal of the 25 nm thick films and shaped via an 8 keV, 120 pA Ga^+ ion beam for milling and an 8 keV, 20 pA Ga^+ ion beam for welding. The further details of the procedure are outlined in [15]–[17]. Upon initial examination, Ga contamination of the specimen was not evident. To encourage the formation of precipitates, the tensile specimen was subjected to a rapid thermal anneal (resistively heated via MEMS capabilities), which encouraged the precipitation of Ga speckling.

The nanostructure of the films was microstructurally characterized through the plane-normal during *in situ* studies in a FEI Tecnai F-20 (S)TEM operated at 200keV. A spot size of 7 was chosen to minimize charging and drift in the device, and bright field conditions were used for *in situ* imaging. All *in situ* data were collected using a OneView camera binned to 2k resolution at one frame per second with drift correction enabled. Data was converted to .TIF files with a reduced bit depth and processed in the Vic-2D software. All images in each data set were

analyzed with reference to the first image collected in that time window. Low-pass filtering and exhaustive search were enabled, and Gaussian subset weights, 8-tap spline interpolation, and the normalized squared difference correlation-criteria were used.

A quick note on selected terminology: in categorizing speckling patterns by clarity, the authors have chosen to use the terms *'clear,' 'faint,'* and *'none.'* Recall that an unpatterned amorphous film, thinned to electron transparency, will often still appear to have some degree of speckling when viewed in various imaging conditions in a TEM [10], [11]. This is the case in the unpatterned C films used in this study. One of the goals of this study is to qualitatively evaluate whether or not an applied speckle patterns improves computer tracking of the translation and deformation of an amorphous film viewed via bright field transmission electron microscopy, particularly given that there is already an inherent speckle pattern in the sample. For this purpose, when the terms *'clear,' 'faint,'* and *'none'* (or *'no'*) are used, they are referring to the applied speckle pattern and not to the inherent amorphous speckle. Regions which are described as having a *'clear'* speckle pattern contain several unmistakable spots of deposited Ga or Pt. A region described as having a *'faint'* speckle pattern appear to have deposited speckles but lack the definite contrast in a *'clear'* pattern. In this *'faint'* pattern, it is difficult to accurately delineate between deposited and native speckling. *'None'* or *'no'* refers to regions containing only native speckling of the amorphous C film.

4.3 Evaluating applied and native speckle patterns

To evaluate the specimen at maximum deformation, the last 100 frames prior to fracture were chosen for analysis. A total of 16 unique sub-regions were selected along the from the video ROI and were each evaluated individually using the Vic-2D software. **Figure 4.1(e)** shows

the entire imaged region of the tensile specimen. Three ROIs are marked inside of **Figure 4.1(e)** which are representative areas that include 'clear', 'faint', and 'no' applied speckle patterns. These regions can be seen at higher magnification in **Figures 4.1(a)-(c)**.

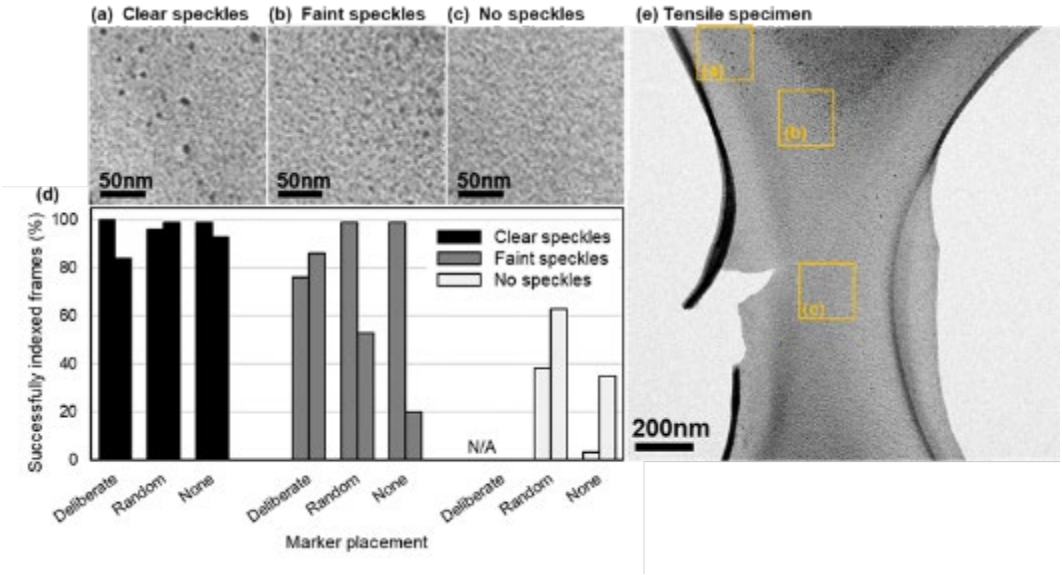

Figure 4.1 (a), (b), and (c) show representative images of regions with a clear speckling pattern, faint speckling pattern, and no speckling pattern, respectively. The bar graph (d) shows the number of successfully indexed frames out of a continuous series of 100 frames as a function of speckle pattern clarity and start point marker placement. Note that the dark edges of the tensile specimen are related to curling behavior in the film.

The Vic-2D software includes a marking tool for identifying starting points for tracking. This is an optional tool designed to optimize the tracking of specific points in the region, particularly in the case of fine or faint speckling [18]. In an effort to improve the odds of successful indexing of the ROI, 6 tracking markers were applied to each ROI. These were applied deliberately to the 'clear' Ga speckling, and randomly to the areas with no speckling. In order to rule out the effects of deliberate vs random placement, other ROIs with 'clear' Ga speckling were also evaluated with randomly placed markers. Finally, to mitigate the influence of qualitative guesswork on what does and does not qualify as a 'clear' speckle pattern, ROIs with 'faint' speckle patterns were also evaluated using both deliberately and randomly placed

markers. In addition to the above, a set of ROIs with ‘clear’, ‘faint’, and ‘no’ speckle patterns were examined using no markers to provide a baseline indicator for the effectiveness of markers in successful tracking and indexing. (The reader should also note that there were no ROIs examined with ‘no’ speckling pattern and deliberately placed tracking markers, as the native speckles were too fine and faint to mark accurately).

Examination of the bar graph in **Figure 4.1(d)** reveals a clear trend in the analyzed data. The addition of Ga speckling does appear to increase the ability of the software to successfully index individual frames in an image series. With this in mind, two larger data sets in the thinnest region were mapped over the same 100 frame time period, i.e., the 100 seconds prior to the specimen fracture. The placement of these ROIs was chosen such that each met several criteria. First, both captured the region which would eventually become the fracture surface, i.e., the region which would be most likely to show deformation behavior. Second, one contained a ‘clear’ speckling pattern across much of the ROI while the other had ‘no’ speckling pattern. Third, the two regions were the same dimensions while still remaining (mostly) in the area of the tensile specimen and also meeting the two above criteria. **Figure 4.2** illustrates the ROIs selected for analysis. It was decided to add starting point markers (a total of 8 per region, deliberately selected for ‘clearly’ speckled ROI and randomly selected for the ROI with ‘no’ speckling), as the data displayed in the bar graph in **Figure 4.1(d)** indicates that there is some improvement in the number of successfully indexed frames when markers are used for this set of images.

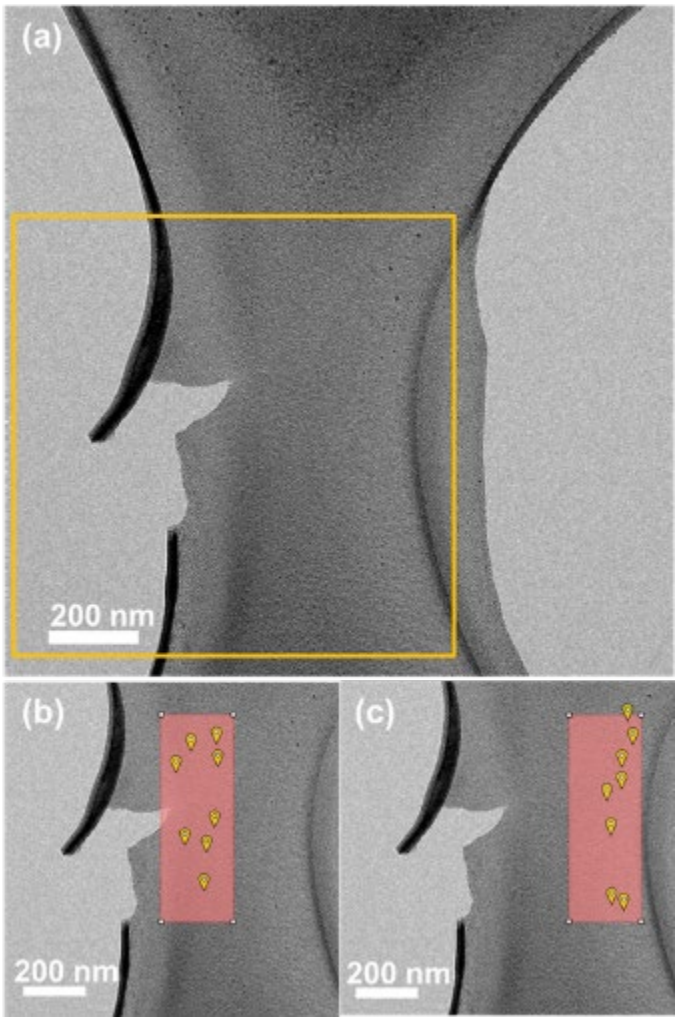

Figure 4.2 Amorphous carbon tensile specimen surface is shown in (a). Marked are randomly selected tracking points in the ROI without Ga speckling (b) and deliberately selected tracking points positioned on Ga speckles (c).

A subset of the resulting displacement maps is presented in **Figure 4.3(a,b)**. Examination of displacement in the $\vec{U}$ direction, **Figure 4.3(a)**, reveals movement of pixels on the left side of the tensile specimen towards center. Likewise, movement of pixels on the right side of the tensile specimen also move towards the center. Together these indicate a contraction of the tensile specimen. Further examination of **Figure 4.3(a)** reveals displacement in the $\vec{V}$ direction that indicates that the top of the specimen is moving upwards while the bottom is pulling downwards. This indicates elongation of the specimen along the tensile direction; combined with the

contraction of the tensile specimen across the width of the specimen, it is clear that the specimen is undergoing necking behavior leading to fracture.

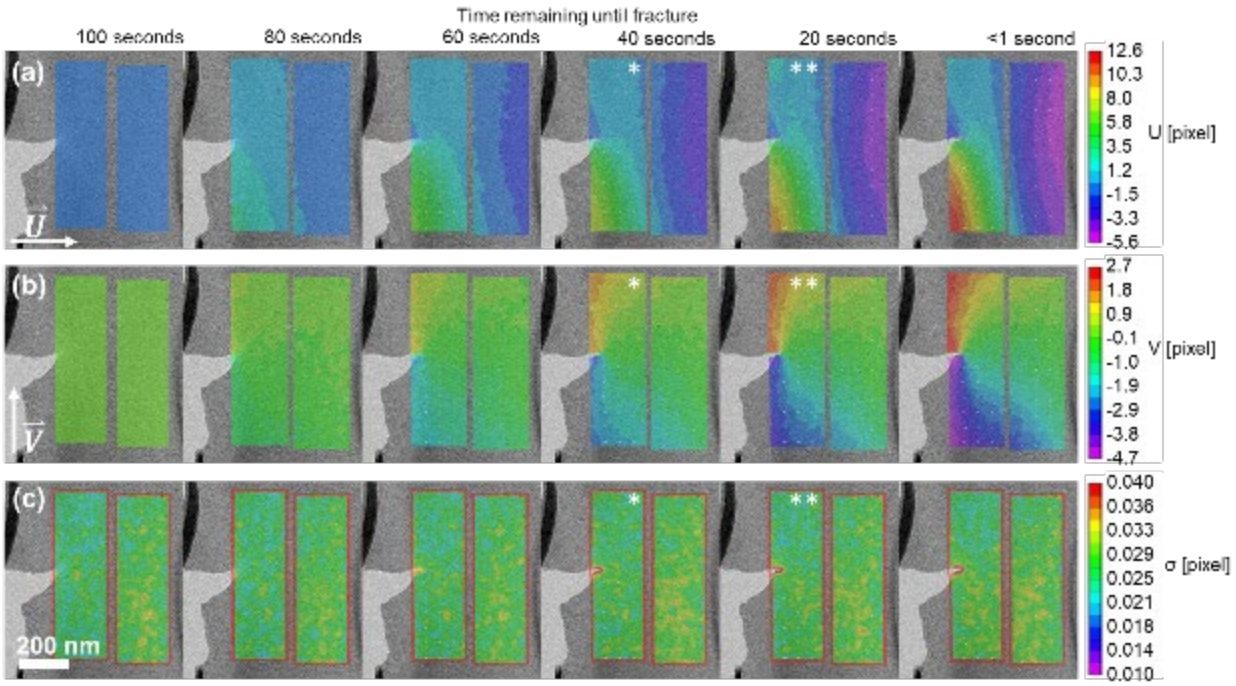

Figure 4.3 Pixel displacements mapped over the 100 second period prior to fracture. The images in (a) and (b) show displacement in the $\vec{U}$ and $\vec{V}$ directions, respectively. Measurement error σ is shown in (c). In each sub image, the right ROI contains Ga speckling while the left ROI does not. Note the ROIs marked by * and ** (40 seconds, left; 20 seconds, left). The exact frames corresponding to the written timestamps were unindexed and were replaced by the nearest adjacent indexed frame (42 seconds, 18 seconds).

Maps of the estimated conference margin (error) is displayed in **Figure 4.3(c)**. For each sub-region, the software calculates a statistical confidence value using the correlation equation. If the confidence region exceeds this threshold, the data will be removed. Error was found to be very low for all indexed frames, as can be seen in the figure. Unindexed frames are thus frames in which error values were higher than the threshold value of 0.050. Less than 50% of frames with 'no' speckling were successfully indexed (**Figure 4.3**, left ROIs), whereas more than 90% of frames with 'clear' Ga speckling (**Figure 4.3**, right ROIs) were indexed. One could increase

this threshold to improve the number of indexed frames, at the potential cost of accuracy in mapping.

Furthermore, the authors would like to discuss the influence of the torn region on error and resulting failure to index. While it is possible that some of the frames which failed to index can be attributed to the exacerbated deformation in the torn section, it should be noted that none of the ROIs used to evaluate the efficacy of applied speckling contained this tear yet had comparable percentages of failed maps. Regardless, from these results it is clear that a native amorphous speckle can be applied to a DIC analysis, and that the addition of an applied pattern such as Ga precipitates can improve the readability of the collected data.

4. Summary

This work examines the application of a fine speckle pattern to an amorphous tensile specimen for DIC analysis of *in situ* deformation behavior in a TEM environment. It was found that the applied Ga speckling pattern improved the ability of the DIC algorithm to successfully index frames and generate displacement maps. In practice, this method of DIC analysis was able to successfully generate displacement maps for an amorphous tensile specimen just prior to fracture, both with applied speckling and with the native amorphous diffraction contrast, revealing an indication of necking behavior that was not immediately visually apparent in the micrographs. However, the percentage of frames that successfully generated displacement maps was greatly increased with the addition of speckling contrast provided by thermally shocked Ga contamination.

Acknowledgements

This work was supported by Army Research Office grant W911NF-17-1-0528. Further, we would like to acknowledge the University of Alabama Analytical Research Center and staff.

References

[1] N. McCormick and J. Lord, “Digital Image Correlation,” *Mater. Today*, vol. 13, no. 12, pp. 52–54, Dec. 2010, doi: 10.1016/S1369-7021(10)70235-2.

[2] J. Górszczyk, K. Malicki, and T. Zych, “Application of Digital Image Correlation (DIC) Method for Road Material Testing,” *Materials*, vol. 12, no. 15, p. 2349, Jul. 2019, doi: 10.3390/ma12152349.

[3] International Digital Image Correlation Society *et al.*, “A Good Practices Guide for Digital Image Correlation,” International Digital Image Correlation Society, Oct. 2018. doi: 10.32720/idics/gpg.ed1.

[4] G. Quino, Y. Chen, K.R. Ramakrishnan, F. Martinez-Hergueta, G. Zumpano, A. Pellegrino, and N. Petrinic, “Speckle patterns for DIC in challenging scenarios: rapid application and impact endurance,” *Meas. Sci. Technol.*, vol. 32, Jul. 2020, doi: 10.1088/1361-6501/abaae8.

[5] A. D. Kammers and S. Daly, “Small-scale patterning methods for digital image correlation under scanning electron microscopy,” *Meas. Sci. Technol.*, vol. 22, no. 12, p. 125501, Dec. 2011, doi: 10.1088/0957-0233/22/12/125501.

[6] H. Schreier, J.-J. Orteu, and M. A. Sutton, *Image Correlation for Shape, Motion and Deformation Measurements*. Boston, MA: Springer US, 2009. doi: 10.1007/978-0-387-78747-3.

[7] A. D. Kammers and S. Daly, “Digital Image Correlation under Scanning Electron Microscopy: Methodology and Validation,” *Exp. Mech.*, vol. 53, no. 9, pp. 1743–1761, Nov. 2013, doi: 10.1007/s11340-013-9782-x.

[8] J. C. Stinville, T. Francis, A.T. Polonsky, C.J. Torbet, M.A. Charpagne, Z. Chen, G.H. Balbus, F. Bourdin, V. Valle, P.G. Callahan, M.P. Echlin, and T.M. Pollock, “Time-Resolved Digital Image Correlation in the Scanning Electron Microscope for Analysis of Time-Dependent Mechanisms,” *Exp. Mech.*, vol. 61, no. 2, pp. 331–348, Feb. 2021, doi: 10.1007/s11340-020-00632-2.

[9] Y. Zhang, L. Feng, S. Dillon, and J. Lambros, “Full-field deformation measurements in the transmission electron microscope using digital image correlation and particle tracking,” *Mater. Charact.*, vol. 183, p. 111598, Jan. 2022, doi: 10.1016/j.matchar.2021.111598.

[10] S. J. Yoo, C.Y. Kim, J.W. Shin, S.G. Lee, J.M. Jeong, Y.J. Kim, S.H. Lee, and J.G. Kim, “Characterization of an amorphous carbon film covering a Mo grid during in situ heating TEM study,” *Mater. Charact.*, vol. 78, pp. 31–36, Apr. 2013, doi: 10.1016/j.matchar.2013.01.011.

[11] D. Di Battista, D. Ancora, G. Zacharakis, G. Ruocco, and M. Leonetti, "Hyperuniformity in amorphous speckle patterns," *Opt. Express*, vol. 26, no. 12, p. 15594, Jun. 2018, doi: 10.1364/OE.26.015594.

[12] X. Wang, Z. Pan, F. Fan, J. Wang, Y. Liu, S. Mao, T. Zhu, and S. Zia, "Nanoscale Deformation Analysis With High-Resolution Transmission Electron Microscopy and Digital Image Correlation," *J. Appl. Mech.*, vol. 82, no. 12, Sep. 2015, doi: 10.1115/1.4031332.

[13] T.-H. Chang and Y. Zhu, "A microelectromechanical system for thermomechanical testing of nanostructures," *Appl. Phys. Lett.*, vol. 103, no. 26, p. 263114, Dec. 2013, doi: 10.1063/1.4858962.

[14] A. Cowen, G. Hames, D. Monk, S. Wilcenski, and B. Hardy, "SOIMUMPs Design Handbook." MEMSCAP Inc, 2011.

[15] L. A. Giannuzzi and F. A. Stevie, "A review of focused ion beam milling techniques for TEM specimen preparation," *Micron*, vol. 30, no. 3, pp. 197–204, Jun. 1999, doi: 10.1016/S0968-4328(99)00005-0.

[16] I. Bikmukhametov, T. R. Koenig, G. J. Tucker, and G. B. Thompson, "A rapid preparation method for in situ nanomechanical TEM tensile specimens," *J. Mater. Res.*, vol. 36, no. 11, pp. 2315–2324, Jun. 2021, doi: 10.1557/s43578-021-00167-9.

[17] M. K. Miller, K. F. Russell, and G. B. Thompson, "Strategies for fabricating atom probe specimens with a dual beam FIB," *Ultramicroscopy*, vol. 102, no. 4, pp. 287–298, Mar. 2005, doi: 10.1016/j.ultramic.2004.10.011.

[18] Correlated Solutions, "Vic-2D: v6 Reference Manual." Accessed: Jun. 09, 2022. [Online]. Available: http://www.correlatedsolutions.com/supportcontent/Vic-2D-v6-Manual.pdf

CHAPTER 5: CONCLUSION

5.1 Summary

Co-based MANCs were evaluated under standard processing conditions (520°C for 20 minutes to establish stable nanocrystalline grains in the amorphous matrix) for the purposes of understanding the relationships between solute content, crystallite nucleation and growth, and microstructure. APT analysis of these alloys reveals that Co and Fe partition preferentially to the crystalline phase, and B, Nb, Si, and Mn segregate to the amorphous matrix. It was also shown that there was improved chemical diffusion with additional solute content, as the chemical partitioning became stronger as more Mn was added. Additionally, it was found that the atomic density in the crystallite phase was increased with higher Mn content; this has been interpreted as being the result of a reduction in defects in the crystalline phase. Review of prior literature [1] revealed a tendency in the binary CoB system for a higher B:Co (which would occur as Co is reduced to balance solute addition) ratio to improve diffusion via an increase in vacancies, implying that such a mechanism could promote mass transport in the as-cast amorphous phase, promoting stronger chemical partitioning and allowing more perfectly ordered crystallites to form. Using this approach, the crystalline integrity can be examined to some extent even under the constraints of the limited spatial resolution in APT.

A second study was then designed to evaluate the nucleation and growth mechanics for this alloy system, and to evaluate the effect of solute addition to those mechanisms. Differential scanning calorimetry was used to evaluate the characteristics of phase transition as a function of solute content, revealing an increase in the necessary energy for the formation of the primary

crystallization phase with higher solute concentrations. From this data, the primary crystallization temperature was estimated to occur around 420°C. To better evaluate crystallite nucleation and growth behavior, the alloys were annealed below this temperature at 400°C to slow crystallization kinetics. Postmortem atom probe tomography and transmission electron microscopy data revealed that the alloy undergoes a constant nucleation condition at these low temperatures as the crystalline volume fraction increases while average crystallite stays the same. Additionally, the compositional profile evolution observed between the as-cast and the 10 minute anneal for the Mn 0.5% alloy implies that the transformation is of a diffusional nature rather than a martensitic transformation. It was also shown that the added solute content suppresses the nucleation and growth behavior of the primary crystallization phase. After longer periods of annealing, coarse boride precipitates began to appear within the alloy; their appearance was delayed in the high Mn sample, implying that their nucleation and growth was also suppressed by the solute content.

Finally, strain annealing has been shown to improve magnetic permeability in these alloys. As the mechanisms responsible for this behavior are not yet understood, a way forward for this work would be *in situ* examination of these alloys as they undergo annealing treatments under load. Current literature applying the principles of DIC to TEM is limited [2], [3]. Chapter 4 described the evaluation of a method for applying digital image correlation techniques to tensile testing in an *in situ* tensile testing environment. Through the FIB liftout process, Ga contamination is naturally introduced to the tensile specimen. This Ga contamination can be made to precipitate via the application of a thermal shock to the specimen, creating a finely dispersed speckle pattern. The efficacy of this applied pattern was then compared with that of the native speckling pattern of an amorphous film imaged in a TEM environment. It was

shown that this applied speckle pattern enhanced the tracking capabilities of the DIC software. It is hoped that this will establish precedent for using finely dispersed speckling patterns to apply DIC analyses to *in situ* tensile testing and eventually, thermomechanical testing of magnetic alloys.

5.2 Recommendations for future studies

Two factors limit current abilities to apply thermomechanical load to these alloys *in situ.* First, available MEMS devices are currently limited to a maximum temperature of 300°C before the integrity of the Si-based device is compromised. Second, it will be necessary to improve techniques for preparing the tensile specimen. Work has been done to sputter these alloys as thin films, onto salt crystals (the current preferred method for the preparation of tensile specimens for these devices), results in an uneven, poorly coalesced film with features unsuitable for DIC analysis. A bright field micrograph of the resulting film can be seen in **Figure 5.1** below.

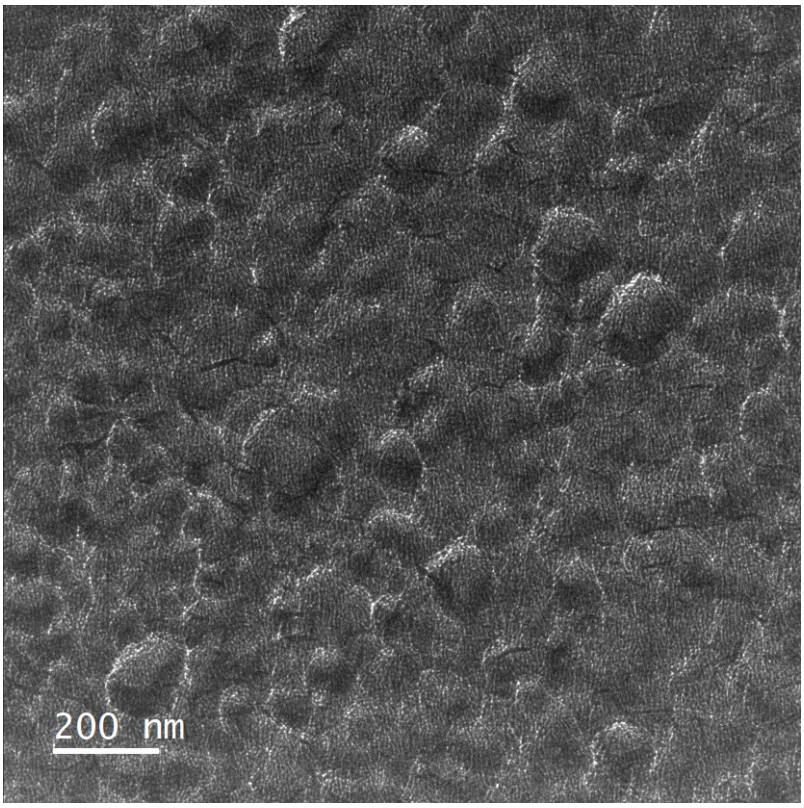

Figure 5.2 The sputter deposited Co MANC takes on the morphology of the salt crystal substrate.

The current recommendation would be to develop a lift-off method from a Si wafer spin coated in photoresist. Other liftout techniques from bulk materials (such as those used for DENS experiments) could also be adapted to be compatible with MEMS geometries. Examination of deformation behavior such as shear banding will be facilitated by the accuracy in strain mapping that DIC can bring to *in situ* testing. Refinement of these techniques will allow the examination of *in situ* thermomechanical testing of MANCs, revealing the influence of applied strain on magnetic properties.

Additionally, the temperature limitation in MEMS devices could be overcome by redesigning them in a different material such as SiC, which would be able to withstand much higher temperatures prior to the deformation of the supporting spring structure. However, this

would require developments device processing and etching techniques for it to become achievable. Alternatively, the original Si-based MEMS device could be used at higher than recommended temperatures with the understanding that each device would then be limited to a single test, and the strain measurements taken during such an experiment would be inaccurate due to plastic deformation of the spring structure. However, such an experiment may still provide valuable information on the MANCs mechanical response during strain annealing.

References

[1] D. K. Belashchenko, V. V. Hoang, and P. K. Hung, “Computer simulation of local structure and magnetic properties of amorphous Co–B alloys,” *J. Non-Cryst. Solids*, vol. 276, no. 1, pp. 169–180, Oct. 2000, doi: 10.1016/S0022-3093(00)00262-3.

[2] Y. Zhang, L. Feng, S. Dillon, and J. Lambros, “Full-field deformation measurements in the transmission electron microscope using digital image correlation and particle tracking,” *Mater. Charact.*, vol. 183, p. 111598, Jan. 2022, doi: 10.1016/j.matchar.2021.111598.

[3] X. Wang *et al.*, “Nanoscale Deformation Analysis With High-Resolution Transmission Electron Microscopy and Digital Image Correlation,” *J. Appl. Mech.*, vol. 82, no. 12, Sep. 2015, doi: 10.1115/1.4031332.

APPENDIX A: EPDF DATA COLLECTION

I. General tips and recommendations

a. Use the same TEM configuration for direct comparisons.

b. Choose an SAED aperture size that is appropriate for the feature of interest. You want to exclude signal contributions from other phases e.g., the Pt cap, Si substrate, etc.

c. Choose a large spot size (≥8). Generally, a larger spot size increases the SNR for high Q areas without saturating the central spot. Note: very high spot sizes with a very small selected area aperture may not provide enough signal.

d. In my experience, binning the image to 1k x 1k during data collection improves SNR and reduces computation time without sacrificing spatial resolution.

Tip: the pattern may be extremely difficult to see on the phosphor screen. Change the monitor brightness to zero and the monitor contrast to ~15 to allow your eyes to adjust to night vision.

Tip: Red light preserves night vision whereas blue/white light disrupts it. A red overlay for the monitor or a red, translucent cover may help in low visibility TEM. I never got this set up but it may be worth looking in to.

II. Data collection procedure

a. Evaluate your sample in the TEM to determine the best SAED aperture size for your sample.

b. Using the aluminum nanoparticle calibration sample (may need to ask Johnny for this), acquire a diffraction pattern using the conditions you selected previously. Use camera length D = 265 mm for acquiring high Q data.

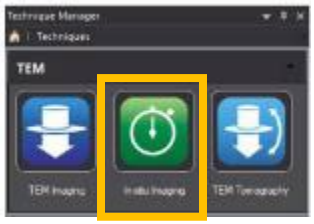

i. This data is best acquired using In-Situ Imaging in Digital Micrograph. I've found that a 1 second exposure time, binned to 1k, is the best option.

ii. You may need to set all binning options to 1 second individually prior to collecting data, as In-Situ data collection can be buggy.

iii. Gather between 20-30 seconds of data, i.e. 20-30 frames. Gathered in quick succession via the In Situ data collection GUI, beam drift should be minimized. Dimmer signals can be acquired for a longer period of time but drift may become a factor.

Tip: Ensure that the TEM is aligned to the best of your abilities here. You will likely be using this calibration file more than once.

Tip: Consider gathering diffraction files for more than one SAED/spot size combination. This may save you time in the future if you find that you need to change your parameters. At the minimum, you will need to adjust the defocus and C2 lens values for each combination.

c. Using the acquired data, calculate the appropriate calibration factor for your chosen conditions (pixel size in $Å^{-1}$)
d. Using the same procedure and TEM configuration, gather data for your sample.
    i. These will be outdated and inaccurate, but my collection parameters were as follows:

SAED aperture	2
Spot size	9
Camera length	265 mm
Defocus	2.39 e-6
Objective	92.2712%
C1 lens	29.945%
C2 lens	45.013%
Exposure time	1 second
Camera binning	1024x1024

III. Data processing procedure
a. Save all files in one folder. I prefer to open the parent folder, search for the data files, and cut/paste them from the results into your desired location.
b. Batch convert all files to .DM3 using Digital Micrograph.

You do not want to have a scale bar in these images; if one appears you will need to edit your data save parameters.
You want to export the image, not the display. Exporting the image preserves all valuable data; exporting the display reduces the bit depth resulting in data loss.

c. Ensure all .DM3 files are in a new folder.
d. Open ePDF suite. See the data file ePDF_Tutorial_ECM29ePDFWorkshop.PDF, which should be included in the program installation files.

IV. Data processing tips
a. You may need to run the centering procedure more than once. Increasing the (x, y) center searching range may reduce the number of iterations needed, but will increase computation time.
b. You will likely want to use [Sum and Integrate] if you have gathered more than one frame. This substantially improves your SNR and your data quality.
c. Ensure that your pixel size and image dimensions are both correct.

d. I've found that generally the program's automated fitting is pretty accurate. Tuning of Qmin is likely necessary; ensure that it is around where you start getting signal (likely just beyond the beam blocker)
e. The graphs of S(a.u.) and F(A^-1) should roughly oscillate about y = 1 and y = 0, respectively. Gentle tuning of R-poly and other parameters can improve this.
f. If the sinusoidal function looks fairly well behaved and bland, it is likely an issue of poor data quality. Ensure that signal is present for high Q values; you will likely need to regather this data.
g. The program does not natively have a great data exporting interface. To export data, export all graphs as all available file formats. In file explorer, make a copy of the file with the extension '*.gr'. Rename the copy with the file extension '*.txt'. You can then import and manipulate the data in Excel/Origin/Matlab/etc.
h. Saving a configuration profile for your project will save you time if you choose to revisit the data. I like to have all of the configuration, mask, and data files saved to one folder for ease of navigation in the future.